The story of a summit nucleus:

Hillslope boulders and their effect on erosional patterns and landscape morphology

in the Chilean Coastal Cordillera

Emma Lodes[1*], Dirk Scherler[1,2], Renee van Dongen,[3] and Hella Wittmann[1]

[1]GFZ German Research Centre for Geosciences, Earth Surface Geochemistry, Telegrafenberg, 14473 Potsdam, Germany

[2]Freie Universität Berlin, Institute of Geographical Sciences, 12249 Berlin, Germany

[3]International Centre for Water Resources and Global Change, 56068 Koblenz, Germany

*Corresponding author (lodes@gfz-potsdam.de)

Key words: [10]Be; cosmogenic nuclides; Chilean Coastal Cordillera; hillslope denudation rates; landscape morphology; grain size; fractures

Abstract

While landscapes are broadly sculpted by tectonics and climate, on a catchment scale, sediment size can influence hillslope denudation rates and dictate the location of topographic highs and valleys. In this work, we used *in situ* [10]Be cosmogenic radionuclide analysis to measure the denudation rates of bedrock, boulders, and soil, in three granitic landscapes with different climates in Chile, with the hypothesis that bedrock and boulders erode slower than soil. To evaluate denudation rates, we present a simple model that assesses differential denudation of boulders and the surrounding soil, considering boulder protrusion. We found that hillslope bedrock and boulders consistently erode more slowly than soil in two out of three of our field

23 sites, which have a humid and a semi-arid climate: denudation rates range from ~5 to 15 m Myr^{-1}

24 for bedrock and boulders and from ~8 to 20 m Myr^{-1} for soil. Furthermore, across a bedrock ridge

25 in the humid site, denudation rates increase with fracture density. In the site with a mediterranean

26 climate, denudation rates for boulders and soil are much higher (~40-140 m Myr^{-1}), likely due to

27 steeper slopes, but the bedrock denudation rate remains low (~22 m Myr^{-1}). Our findings suggest

28 that bedrock patches and large hillslope boulders affect landscape morphology through inducing

29 differential denudation. When occurring long enough, such differential denudation should lead to

30 topographic highs and lows controlled by bedrock exposure and hillslope sediment size. Based on

31 analysis of high-resolution digital elevation models of our field sites, we observe that streams

32 follow the orientation of at least one major fault orientation. We thus infer that bedrock fracture

33 patterns set maximum grain sizes in our field sites, thus influencing hillslope denudation and

34 stream incision.

35 **1   Introduction**

36   Landscapes on Earth are shaped by tectonic uplift and climate, which dictate erosional

37 and weathering regimes over geologic timescales. When uplift and climate are held constant

38 sufficiently long, fluvial landscapes reach a steady state, in which the slopes of hills and stream

39 channels adjust so that denudation rates match tectonic uplift rates (e.g. Burbank et al., 1996;

40 Kirby and Whipple, 2012). Variations in bedrock strength and the grain size of hillslope

41 sediment, however, exert additional control on the morphology of hills and valleys (e.g. Attal et

42 al., 2015; Glade et al., 2017). Initially, hillslope sediment size is set by lithology and the density

43 of fractures, which are formed due to tectonic and topographic stresses (e.g. Molnar et al., 2007;

44 St. Claire et al., 2015; Roy et al., 2016; Sklar et al., 2017). Near the earth surface, water, often

45 carrying biotic acids, infiltrates bedrock fractures and promotes chemical weathering that further

46 reduces sediment size and converts bedrock to regolith (Lebedeva and Brantley, 2017; Hayes et

47 al., 2020). Therefore, long residence times of sediment in the weathering zone (on a million-year

48 timescale), being the consequence of slow erosion, may result in complete disintegration of

49 bedrock and the formation of saprolite and soil, whereas rapid erosion and short residence times

50 can lead to hillslope sediment size limited by fracture spacing (e.g. Attal et al., 2015; Sklar et al.,

51 2017; Roda-Boluda et al., 2018; Verdian et al., 2021). A spectrum between these end-members

52 can also exist within one catchment, especially where variations in lithology, fracture density or

53 elevation cause spatial differences in the rate and/or extent of weathering (e.g. Sklar et al., 2020).

54 Where weathering does not completely disintegrate the bedrock, boulders, or corestones, can be

55 found embedded in hillslope sediment, with a maximum size set by the spacing of bedrock

56 fractures (Fletcher and Brantley, 2010; Buss et al., 2013; Sklar et al., 2017). Here we focus on the

57 effects of such boulders on differential denudation and landscape morphology on hillslopes with

58 mixed cover of soil, boulders and bedrock.

59   Soil-mantled hillslopes are typically considered to be dominated by diffusive processes,

60 for which conceptual models and geomorphic transport laws are relatively well-established (e.g.,

61 Dietrich et al., 2003; Perron, 2011). However, these models generally assume uniform hillslope

62 material and do not account for the exhumation of larger boulders through the critical zone. Neely

63 et al. (2019) recently addressed erosion and soil transport on mixed bedrock and soil-covered

64 hillslopes using a nonlinear diffusion model, but assumed the same denudation rate for bedrock

65 and soil. Fletcher and Brantley (2010) modeled the reduction in the size of corestones due to

66 chemical weathering as they are exhumed through the weathering zone, although this model does

67 not consider the corestones' effect on differential erosion. Often, however, bedrock and large

68 boulders protrude above the surrounding soil, indicating that they are eroding more slowly than

69 the soil. Indeed, studies have shown that average denudation rates of bedrock outcrops and

70   hillslope boulders are often lower than catchment average and soil denudation rates (e.g.

71   Bierman, 1994; Heimsath et al., 2000; Granger et al., 2001; Portenga and Bierman, 2011).

72   Larger boulders require greater forces to be moved, which can be achieved by steepening

73   slopes (Granger et al., 2001; DiBiase et al., 2018; Neely and DiBiase, 2020), or by lengthening

74   residence time until subaerial weathering has decreased their size sufficiently to be transported

75   downslope. During this prolonged residence time, boulders can shield hillslopes from erosion

76   (Glade et al., 2017; Chilton and Spotlia, 2020), and stream channels from incision (Shobe et al.,

77   2016; Thaler and Covington, 2016). In terrain where spatial gradients in bedrock fracture spacing

78   result in spatial gradients of hillslope sediment size, it is thus reasonable to expect that the

79   resistance of surface boulders to weathering and transport ought to retard erosion locally,

80   resulting in spatially differential erosion. Moreover, because smaller blocks are also more easily

81   transported in fluvial systems (Shobe et al., 2016), we would expect that rivers preferentially

82   incise in zones of more intensely fractured rocks (Buss et al., 2013) that align with the orientation

83   of faults (Molnar et al., 2007; Roy et al., 2016).

84   In this study we provide a new framework for measuring and assessing differential

85   denudation of boulders and the surrounding fine-grained regolith on hillslopes, and also discuss

86   the extent to which bedrock fracturing affects sediment size, denudation rates, and stream

87   incision. We quantified bedrock, boulder, and soil denudation rates in three different areas along

88   the granitic Coastal Cordillera of Chile with different climates and erosional regimes, using *in*

89   *situ* cosmogenic ^{10}Be. By developing a simple model to convert ^{10}Be concentrations from

90   boulders into soil and boulder denudation rates, we explored the hypothesis that on a hillslope,

91   boulders affect differential erosion by eroding more slowly than the surrounding soil, with the

92   corresponding null hypothesis that no difference exists between soil and boulder denudation rates.

93   We make the simplifying assumption that soil denudation rates remain constant over the time

94   period that a boulder is exhumed, and over long time periods, denudation rates throughout the

95   landscape vary according to whether boulders or soil are exposed at the surface. Following the

96   logic outlined above, we additionally examined our field sites for signs of fracture control on

97   landscape morphology with the hypothesis that more highly fractured bedrock is more susceptible

98   to denudation and stream incision than intact bedrock.

99   **2   Field sites**

100   The Chilean Coastal Cordillera, a series of batholiths in the forearc of the Andean

101   subduction zone, lies along a marked climate gradient with humid conditions in the south and

102   hyper-arid conditions in the north (Fig. 1). The Andean subduction zone, in which the Nazca

103   Plate subducts under the South American Plate, has been active since at least Jurassic times (e.g.,

104   Coira et al., 1982). In this study we investigated three field sites along the Coastal Cordillera from

105   south to north: Nahuelbuta National Park, (NA), with a humid-temperate climate, La Campana

106   National Park (LC), with a mediterranean climate, and Private Reserve Santa Gracia (SG), with a

107   semi-arid climate (Fig. 1). NA and SG have mostly convex, diffusively-eroding hillslopes, while

108   hillslopes in LC are steeper and landslides have been observed (van Dongen et al., 2019; Terweh

109   et al., 2021). All three sites are underlain by granitoid bedrock (Oeser et al., 2018), none show

110   any signs of former glaciation, and all are located on protected land, away from major human

111   influence, such as mines, dams, and large infrastructure. In all three sites, denudation rates from

112   [10]Be cosmogenic radionuclide analysis have been reported by van Dongen et al. (2019)

113   (catchment average rates), and Schaller et al. (2018) (soil pits).

114   NA is located on an uplifted, fault-bounded block (plateau), an unusually high part of the

115   Coastal Cordillera with a mean elevation of ~1300 m above sea level. Tectonic uplift rates in NA

116   increased from 0.03–0.04 to >0.2 mm year^{-1} at 4±1.2 Ma (Glodny et al., 2008), a shift that

117   appears to be also recorded by knickpoints in streams that drain the plateau. All of the

118   measurements in this work are from the plateau (~9° mean slope), above knickpoints. ^{10}Be-

119   derived denudation rates are around 30 m Myr^{-1} (Schaller et al., 2018; van Dongen et al., 2019),

120   indicating that denudation rates on the NA plateau have not yet adjusted to the higher uplift rates.

121   The main catchment in LC has a mean elevation of 1323 m with a mean slope of 23°, and

122   regional uplift rates are estimated to be <0.1 mm yr^{-1} (Melnick, 2016). Van Dongen et al. (2019)

123   reported a catchment average denudation rate of ~200 m Myr^{-1} for a sub-catchment in LC,

124   whereas Schaller et al. (2018) reported soil denudation rates of 40-55 m Myr^{-1}. In SG, the mean

125   elevation is 773 m above sea level, the mean slope is 17.2°, and uplift rates are <0.1 mm year^{-1}

126   (Melnick, 2016). Previously reported ^{10}Be-derived denudation rates are ~9-16 m Myr^{-1} (Schaller

127   et al., 2018; van Dongen et al., 2019).

128   **3   Methods**

129   **3.1   In situ ^{10}Be analysis**

130   **3.1.1   Sample collection**

131   We collected samples for cosmogenic ^{10}Be analysis from bedrock, boulders, and soil to

132   estimate denudation rates in our field sites, targeting hillslopes near previously-collected

133   catchment average and soil pit samples from van Dongen et al (2019) and Schaller et al. (2020).

134   All sample locations are shown in Figure 1. Bedrock samples were taken using a hammer and

135   chisel from an area of up to ~20 m × 20 m (on ridge tops or hillslopes) and consist of an

136   amalgamation of at least ten chips (~25 cm^2 and <2 cm thick), with which we aim to obtain

137   representative mean values of denudation rates that are potentially variable due to episodic

138   erosion by spalling rock chips (Small et al., 1997). Similarly, for boulder samples, one chip was

139   taken from the top of each of at least ten similarly-sized boulders and amalgamated for an area of

140   up to ~40 m × 40 m, depending on boulder abundance. We targeted boulders that appear to be in

141   situ (essentially, exhumed corestones), based on the observation that they are tightly imbedded in

142   the ground. We acknowledge that it is possible that some of the larger sampled boulders are

143   connected to bedrock roots, and that it is also possible that some boulders are not in situ, despite

144   our best efforts. In places with many various-sized boulders, we collected samples from different

145   protrusion heights (~1-m tall boulders, ~0.5-m tall boulders, etc.). Each sampled boulder was

146   measured along the a, b, and c axes, as far as discernible (see Table 1). We also measured the

147   protrusion height of each boulder from the center of the top of the boulder to the ground. Each

148   protrusion height value in Table 1 consists of an average of at least ten boulders of similar

149   protrusion heights that we sampled for one amalgamated sample. Boulders on sloping surfaces

150   typically show varying protrusion heights, with higher values downslope and lower values

151   upslope. In such cases, we measured protrusion at the sides of boulders. Occasionally, we

152   observed that upslope protrusion was further reduced by sediment trapping upslope of boulders.

153   Topsoil samples were also collected by amalgamation in the area surrounding the sampled

154   boulders.

155   In NA, we collected five bedrock samples from an area called Piedra de Aguila from

156   outcrops with different fracture densities, and measured fracture spacing by stringing a measuring

157   tape along the bedrock surface and measuring the distance between fractures that were at least 1

158   mm wide (Fig. 2A1 and 2A2). We further collected six boulder samples and three soil samples

159   from the ridge and hillslope of Cerro Anay (Fig. 2A3), an area called Casa de Piedras, and a

160   hillslope near the soil pits that were sampled by Schaller et al. (2018). In LC and SG, we were not

161   able to collect samples at variably fractured bedrock outcrops due to rarely exposed bedrock. In

162   LC, we took one bedrock sample, two boulder samples and two soil samples from the ridge and

163   slope of Cerro Cabra (Fig. 2B1), and three boulder samples and three soil samples from the ridge,

164   upper slope, and lower slope of Cerro Guanaco (Fig. 2B3). In SG, we took four boulder samples

165   and three soil samples from the ridge and slope of Santa Gracia Hill, which also hosts the soil pits

166   of Schaller et al. (2018) (Fig. 2C2 and 2C3), and two boulder samples and one soil sample from

167   the ridge of Zebra Hill (Fig. 2C1).

168   **3.1.2   Analytical methods**

169   We dried, crushed, and sieved amalgamated bedrock and boulder samples for quartz

170   mineral separation, and dried and sieved soils, each to 250-500 micrometer particle size, or to

171   250-1000 micrometers if the 250-500 micrometer sample amount wasn't sufficient. We used

172   standard physical and chemical separation methods to isolate ~20 g of pure quartz from each

173   sample. After spiking each sample with 150 μg of ^{9}Be carrier and dissolving the quartz in

174   concentrated hydrofluoric acid, we extracted Be following protocols adapted from von

175   Blanckenburg et al. (2004). ^{10}Be/^{9}Be$_{(carrier)}$ ratios were measured by accelerator mass

176   spectrometry at the University of Cologne, Germany (Dewald et al., 2013). Sample ratios were

177   normalized to standards KN01-6-2 and KN01-5-3 with ratios of 5.35×10^{-13} and 6.320×10^{-12},

178   respectively. Final ^{10}Be concentrations were corrected by process blanks with an average

179   Be^{10}/Be$^9_{(carrier)}$ ratio of $(2.21 \pm 0.25) \times 10^{-14}$.

180   **3.1.3   Denudation rate calculations**

181   In order to calculate denudation rates from the measured ^{10}Be concentrations, we

182   evaluated bedrock, boulder, and soil samples differently. Bedrock samples present the simplest

183   case, in which we assumed steady state erosion and calculated bedrock denudation rates (ϵ_{br})

184   using the CRONUS online calculator v2.3 (Balco et al., 2008). The steady state assumption is

185   based on our amalgamated sampling, and follows the results of Small et al. (1997), who showed

186   that an amalgamation of several individual bedrock samples is a reasonable approximation of the

187   long-term average denudation rate in episodically eroding settings.

188   Boulder and soil samples require a more nuanced assessment. Boulders protrude above

189   the ground surface, which implies that the lowering of the ground surface (i.e., the soil

190   denudation rate, ϵ_s) is faster than the lowering of the boulder's surfaces (i.e., the boulder

191   denudation rate, ϵ_b) (Fig. 3). Thus, even while they are buried and covered by soil (or saprolite),

192   boulders are exposed to cosmic rays for a significant amount of time prior to breaching the

193   surface (Fig. 3A). We refer to this time span as phase 1. When boulders breach the surface, they

194   should have a concentration similar to that of the surrounding soil (Fig. 3B). As boulders are

195   exposed during phase 2, nuclide production and decay continues, but it takes time for the boulder

196   surfaces to attain a [10]Be concentration that is in equilibrium with the slower boulder denudation

197   rate. Thus, we expect that the measured concentrations from the tops of boulders are

198   combinations of the two different phases in which [10]Be is accumulated at different rates (first a

199   rate corresponding to the soil denudation rate, and after exhumation, a rate corresponding to the

200   boulder denudation rate). Converting the [10]Be concentrations of soil samples collected from

201   around the boulders to a denudation rate also requires a special approach, as these samples

202   include an unknown number of grains eroded off boulders, which ought to increase the [10]Be

203   concentration, due to the slower denudation rate of boulders, as compared to soil.

204   Because of the above complications, we used an approach to estimate the soil and boulder

205   denudation rates that considers the measured boulder protrusion heights and their measured [10]Be

206   concentrations. We modelled [10]Be concentrations ($N_{modelled}$, in atoms g^{-1}) by approximating the

207   production rate profile with a combination of several exponential functions (e.g., Braucher et al.,

208   2011) during the two different phases:

$$N_{modelled} = \sum_i \frac{P_i(0)}{\lambda + \frac{\epsilon_s \rho}{\Lambda_i}} e^{-t_2\lambda} + \sum_i \frac{P_i(0)}{\lambda + \frac{\epsilon_b \rho}{\Lambda_i}} \left[1 - e^{-t_2\left(\lambda + \frac{\epsilon_b \rho}{\Lambda_i}\right)} \right] \qquad (1),$$

209   where i indicates different terms for the production by spallation, fast muons, and negative

210   muons; $P_i(0)$ are the site-specific [10]Be surface production rates in atoms g[-1] yr^{-1} for the different

211   production pathways (Table 1); λ is the [10]Be decay constant (4.9975×10^{-7}); ϵ_b is the boulder

212   denudation rate (cm yr^{-1}); and Λ_i is the attenuation length scale (160 g cm^{-2} for spallation, 4320 g

213   cm[-2] for fast muons, and 1500 g cm^{-2} for negative muons, respectively; Braucher et al., 2011). ρ is

214   the boulder density, and here we use a value of 2.6 g cm^{-3} for all samples. Although the density of

215   soil and saprolite layers would be lower, we do not have information on the thickness of these

216   layers at each field site, and soil depth is often highly variable throughout granitic landscapes

217   (e.g. Callahan et al., 2020). In addition, we do not have information about the material that has

218   already eroded from around the evaluated boulders (Balco et al., 2011). Surface production rates

219   by spallation are based on a SLHL (sea level high latitude) reference production rate of 4.01

220   atoms g[-1] yr^{-1} (Borchers et al., 2016) and the time-constant spallation production rate scaling

221   scheme of Lal (1991) and Stone (2000) ('St' in Balco et al., 2008). Surface production rates by

222   both fast and negative muons were obtained using the MATLAB-function 'P_mu_total.m' of

223   Balco et al. (2008). Topographic shielding at each sampling site was calculated with the function

224   'toposhielding.m' of the TopoToolbox v2 (Schwanghart and Scherler, 2014) and 12.5-meter

225   resolution ALOS PALSAR-derived digital elevation models (DEMs) from the Alaska Satellite

226   Facility.

227   In equation 1, the first term represents phase 1 and the second term represents phase 2,

228   with t_2 being the exposure time of the boulder, calculated from the height of the boulder (z)

229   divided by the difference between the soil denudation rate and the boulder denudation rate:

$$t_2 = \frac{z}{(\epsilon_s - \epsilon_b)} \qquad (2)$$

230   For each sample and associated average boulder protrusion height, we modelled [10]Be

231   concentrations with equation 1 for different combinations of soil and boulder denudation rates

232   that we allowed to vary between 5 and 50 m Myr^{-1} (NA), between 3 and 50 m Myr^{-1} (SG), and

233   between 10 and 300 m Myr^{-1} (LC), guided by previously published denudation rate estimates

234   (Schaller et al., 2018; van Dongen et al., 2019). We consider permissible denudation rates as

235   those for which the difference between the modelled and observed [10]Be concentrations is less

236   than the measured 2σ concentration uncertainty.

237   This idealized model rests on several assumptions; 1) the landscapes are in a long-term

238   steady state where denudation is locally variable as boulders and bedrock are exhumed in

239   different locations, but this variation is around a long term stable average; 2) soil denudation rates

240   remain steady over the course of boulder exhumation; 3) boulders are in situ and have not rolled

241   downhill, and 4) boulder have not been intermittently shielded during their exhumation.

242   Assumptions 3 has a higher chance of being violated on steep slopes or where boulders are tall,

243   and assumption 4 is more likely violated where boulders are densely clustered. These scenarios

244   are discussed in more detail in section 5.1.

245   **3.2   Topographic analysis**

246   To test if stream orientations in our field sites follow fault orientations, we analyzed the

247   orientations of streams using one-meter resolution LiDAR DEMs (Kügler et al., 2022). Within

248   each DEM, we first calculated stream networks based on flow accumulation area thresholds of

249   10^4, 10^5 and 10^6 m^2. The lowest threshold was determined based on the occurrence of incised

250   channels visible in the DEMs. We then used the TopoToolbox function 'orientation' with a

251   default smoothing factor (*K*) of 100, to obtain the orientation of each node in the stream network.

252 Fractures in the field can only be seen where there are bedrock outcrops, which are generally

253 scarce. Therefore, we decided to refer to the orientation of faults, as depicted in geological maps,

254 with the assumption of similar orientation (Krone et al., 2021; Rodriguez Padilla et al., 2022). To

255 obtain the orientation of mapped faults, we extracted faults within ~50 km of each sampling site

256 from a 1:1,000,000-scale geological map from Chile's National Geology and Mining Service in

257 ArcGIS (SERNAGEOMIN, 2003). Fault orientations were measured for straight fault segments

258 with a length of 100 m. Because we are only interested in the strike of streams and faults, all

259 orientations lie between 0° and 180°. For displaying purposes in rose diagrams, we mirrored these

260 values around the diagram origin by duplicating values and adding 180°.

261 **4   Results**

262 **4.1 ^{10}Be concentrations**

263   Measured ^{10}Be concentrations span a wide range of values, and are generally lowest in LC

264 and higher in NA and SG (Table 1). Within NA, we observe the lowest averaged ^{10}Be

265 concentrations (normalized to SLHL) for soil samples ($\mu \pm 2\sigma = 1.41\times10^5\pm0.06\times10^5$ atoms g^{-1}),

266 followed by bedrock samples ($2.19\times10^5\pm0.07\times10^5$ atoms g^{-1}) and boulder samples

267 ($2.82\times10^5\pm0.08\times10^5$ atoms g^{-1}) (Fig. 4A). In NA at Piedra de Aguila, where we were able to

268 measure fracture spacing in areas with exposed bedrock, the ^{10}Be concentrations of samples from

269 fractured bedrock decrease with increasing fracture density (Fig. 5A). One boulder sample from

270 the slope of Soil Pit Hill stands out with a concentration that is lower than most soil samples.

271 Similar, but slightly higher average values as in NA are attained in SG, with soil samples

272 ($2.24\times10^5 \pm 0.11\times10^5$ atoms g^{-1}) being lower than boulder samples ($4.22\times10^5 \pm 0.16\times10^5$ atoms g^{-}

273 ^{1}) (Fig. 4C). Only in LC are the differences between averaged soil ($0.82\times10^5 \pm 0.04\times10^5$ atoms g^{-}

274 ^{1}) and boulder samples ($0.74\times10^5 \pm 0.05\times10^5$ atoms g^{-1}) small, and with 2σ error, within

275   uncertainties (Fig. 4B). In addition, at 3 out of 5 sampling locations in LC, boulders have lower

276   concentrations than adjacent soil samples, inconsistent with the assumption that $\epsilon_s < \epsilon_b$ (see

277   section 3.1.3). However, our single bedrock sample from LC has a higher concentration of

278    $1.38 \times 10^5 \pm 0.16 \times 10^5$ atoms g^{-1}. In NA and SG, boulder samples from slope locations have lower

279   average ^{10}Be concentrations compared to boulder samples from ridge locations. Again, in LC this

280   pattern does not hold. Finally, we do not observe a significant trend between ^{10}Be concentration

281   and protrusion height (Fig. 5C); however, there is a relationship between protrusion height and

282   slope for LC (Fig. 5D).

283   **4.2   Bedrock, boulder, and soil denudation rates**

284   Bedrock denudation rates in NA range from 8.53 ± 0.60 m Myr^{-1} to 18.64 ± 1.40 m Myr^{-1},

285   and the LC bedrock sample yielded a denudation rate of 22.28 ± 2.62 m Myr^{-1}. We modelled

286   boulder (ϵ_s) and soil denudation rates (ϵ_s) using the approach described in section 3.1.3 for all

287   boulder samples that have higher concentrations than the adjacent soil concentrations. We address

288   locations where ^{10}Be concentrations are higher in soil compared to boulder samples in the

289   discussion (three locations in LC and one in NA). In contrast to the bedrock denudation rates,

290   modelled boulder and soil denudation rates have no unique solution, and their ranges of possible

291   denudation rates are more complex (Fig. 6). The ranges of denudation rates, illustrated by the

292   curves in Fig. 6, are comprised of values for which the difference between the measured and

293   modelled ^{10}Be concentrations are less than the measured 2σ ^{10}Be concentration uncertainty,

294   where modelled ^{10}Be concentrations are based on Eq. 1. Each colored band represents one

295   amalgamated boulder sample (such as 1-meter-protruding boulders from the ridge of Cerro

296   Anay). The x-axis shows the range of modelled boulder denudation rates, and the y-axis shows

297   the range of modelled soil denudation rates. However, not every combination within the range

298   plotted in Fig. 6 is plausible. For example, the part of the colored bands in Fig. 6 that is close to

299   the 1:1-line (edge of the gray area) exists because at very low differential denudation rates

300   (differences between soil and boulder denudation rates), phase 2 gets very long so that the

301   boulder denudation rate dominates the resulting concentration and approaches the value one

302   would obtain when neglecting the first term on the right side in Eq. 1. We argue that differential

303   denudation rates of less than ~1 m Myr^{-1} are highly unlikely, as it would take ~1 Myr to exhume a

304   boulder of only 1 m in height above the soil, while simultaneously eroding many times more soil

305   and boulder material.

306   In NA, permissible modelled soil denudation rates range from ~13 to 37 m Myr^{-1} and

307   permissible modelled boulder denudation rates range from ~5 to 20 m Myr^{-1} (Fig. 6A). Three

308   samples that were taken from the same ridge at Cerro Anay (Fig. 2A3 and 4A) all overlap in

309   denudation rate despite varying protrusion heights. These samples also overlap with a sample

310   from Casa de Piedras, and together indicate a rather narrow range of soil and boulder denudation

311   rates of ~15-20 m Myr^{-1} and ~10-15 m Myr^{-1}, respectively. Only the mid-slope sample from

312   Cerro Anay has higher modelled soil and boulder denudation rates. In LC, modelled boulder and

313   soil denudation rates that are consistent with the measured [10]Be concentrations extend to much

314   higher values compared to the other field sites (40-140 m Myr^{-1}; Fig. 6B) and the two solutions

315   do not overlap. In SG, permissible modelled denudation rates are similar in magnitude to results

316   from NA (Fig. 6C); soil denudation rates range from ~7 to 28 m Myr^{-1} and boulder denudation

317   rates range from ~4 to 23 m Myr^{-1}. Samples taken from the ridge of Santa Gracia Hill (Fig. 2C2

318   and 4C) have permissible modelled soil and boulder denudation rates that overlap at values of

319   ~12-15 m Myr^{-1} and ~10-12 m Myr^{-1}, respectively, whereas samples from the ridge of Zebra Hill

320   overlap at ~4-5.5 m Myr^{-1} for boulders and ~6.5-7.5 m Myr^{-1} for soil. Samples from the slope of

321   Santa Gracia Hill have higher modelled soil denudation rates, when considering very low

322   differential denudation rates unlikely. We further discuss the most plausible ranges of denudation

323   rates in sections 5.1 and 5.2.

4.3   Fault and stream orientations

325   Fault orientations in our field sites, based on straight segments of 100 m (8,731 segments

326   for SG, 6,572 segments for LC, and 6,214 segments for NA), generally have at least one

327   dominant orientation that aligns with stream orientations (Fig. 7). Stream orientations depend on

328   the flow accumulation threshold: at smaller thresholds (10^4 m^2), abundant small streams yield a

329   wide distribution of orientations that seems to reflect the shape of the catchment as a whole. At a

330   high flow accumulation threshold (10^6 m^2), the derived stream networks comprise only the largest

331   channels and their orientation is strongly controlled by the orientation and tilt of the drainage

332   basin. This can be seen clearly in NA, where the east-west oriented trunk stream is weighted

333   heavily. In SG, faults and stream orientations match each other well, both trending north-south. In

334   LC and NA, one of two regional fault orientations matches stream orientations, and faults closest

335   to the field sites more closely match dominant stream orientations (red faults in Fig. 7).

336   Specifically, in LC, the dominant orientations for the regional faults are roughly northeast and

337   secondarily northwest, whereas streams are generally oriented northwest. In NA, faults generally

338   have east-west and northwest-southeast orientations, and streams with an accumulation threshold

339   above 10^4 follow an east-west orientation.

5   Discussion

5.1   Deciphering the denudation rates of boulders and soil

342   Our model results show that there exist no unique combination of soil and boulder

343   denudation rates for any particular site (Fig. 6). Which, then, are the most plausible combinations

344   of boulder and soil denudation rates? The answer depends on the characteristic exhumation

345   histories of the boulders, and events that could have influenced the accumulation of ^{10}Be during

346   the course of exhumation. In order to narrow down the ranges of denudation rates for boulders

347   and soils investigated in this study, we address several complicating factors, such as shielding and

348   toppling of boulders, and compare measured and modelled ^{10}Be concentrations of soils to each

349   other.

350   **5.1.1   Shielding and toppling of boulders**

351   There exist two scenarios to inadvertently introduce bias into our approach of determining

352   boulder denudation rates: (1) sampling of boulders that have been previously shielded by soil or

353   other boulders, and (2) sampling of boulders that have toppled or rolled downhill, and that are no

354   longer in situ. In either case, the actual production rate for the sample would be lower than

355   assumed, leading to an artificially high denudation rate estimate. Shielding by boulders is more

356   likely in areas where there are tall, densely-clustered boulders, or at protruding bedrock outcrops

357   such as Piedra de Aguila, where we measured a very low ^{10}Be concentration in sample NB-BR4

358   (Table 1; Fig. 4A). This sample was taken from a bedrock knob close to a cliff in an area

359   accessed by tourists; it is possible that the low concentration of our sample is due to shielding by

360   boulders that toppled, or were manually moved from the sampled area.

361   Boulders in steeply sloping areas are more likely to be shielded by soil or topple downhill.

362   In LC, where slopes are generally steeper than the other field sites, it is possible that some

363   boulders were not in situ when we sampled them: they could have rolled or been overturned on

364   the steep slopes, uncovering a side that was previously shielded. They could have also been

365   transiently shielded by soil coming from upslope (Fig. 2B3). In addition, there is a significant

366   relationship between protrusion height and hillslope angle for LC boulders, indicating that

367   boulders on steeper slopes are either smaller, or may be partially buried by upslope soil (Fig. 5D).

368   Indeed, three boulder samples from LC (LC2, LC4, and LC18; Table 1) have measured ^{10}Be

369   concentrations that are lower than the surrounding soil, violating our model assumptions, and

370   suggesting that the sampled boulder surfaces were shielded. Two of these amalgamated boulder

371   samples (LC4 and LC18) were collected from slopes with rather high angles of 27° and 18°,

372   respectively, and therefore could include toppled boulders. Boulder sample LC2 however was

373   collected on a ridge with a relatively lower slope of 9° (Table 1). In that case, the low ^{10}Be

374   concentration could stem from shielding by stacked boulders (scenario 1). In NA, one boulder

375   sample (NA15; Table 1) also has a very low ^{10}Be concentration and was not included in the

376   model. We did not collect a soil sample near the boulder sample NA15, and instead compared its

377   concentration to the adjacent surficial soil pit sample of Schaller et al. (2018). Because these

378   samples were not taken exactly next to each other, there exists some ambiguity in this

379   comparison. However, the relatively low ^{10}Be concentration of sample NA15 when compared to

380   other boulder samples in NA suggests issues that could be related to shielding or toppling of

381   boulders. Over long timescales, we expect all sampled boulders to be fully exhumed and either

382   weather away completely in place or topple down the hill, eventually ending up in streams where

383   they would be exported from the catchment at a later stage. It is plausible that such a cycle of

384   boulder exposure, exhumation, and transport has operated in the past and will continue into the

385   future. In LC, due to higher hillslope angles and overall higher denudation rates, this cycle seems

386   to be occurring at a faster rate, probably leading to a higher chance of sampling boulders that

387   have more recently been exhumed and rolled downhill.

5.1.2 Plausible ranges for modelled denudation rates

388

389   For most of our soil samples, measured ^{10}Be concentrations agree well with modelled

390   ^{10}Be concentrations (Table 2), suggesting the model assumptions to be reasonable. Positive or

391   negative deviations are expected, however, because (1) soil samples we collected in the field are

392   most likely a mixture between lower concentration soil that is directly exhumed from below, and

393   higher concentration grains eroded from the surrounding boulders, (2) soil surrounding boulders

394   could be blocked from moving downslope by the boulders themselves (as shown in Glade et al.,

395   2017), which could slow down soil transport and raise soil ^{10}Be concentrations, (3) we did not

396   account for shielding of soil by the surrounding boulders, which would lower production rates,

397   and (4) the density of material that eroded from around boulders as they were exhumed could

398   have been lower or variable, whereas for the model we used a uniform density for boulders and

399   soil. If case 4 were true, the modelled soil denudation rates would be lower than they should be

400   (or modelled soil concentrations would be higher than they should be). However, in most cases,

401   the modelled soil concentrations are slightly lower than the measured soil concentrations, which

402   suggests that cases 1 or 2 are common in our field sites. In one case (Casa de Piedras in NA), the

403   measured soil ^{10}Be concentration is significantly lower than the modelled soil ^{10}Be concentration

404   (Table 2). If the soil was eroding as fast as our measured soil samples indicate, the boulders

405   should be protruding higher. However, Casa de Piedras has a high density of tall boulders. The

406   observed discrepancy could be caused by boulders shielding the soil directly surrounding it from

407   cosmic rays, or by eroding chips with low ^{10}Be concentrations of shielded parts of the boulders,

408   perhaps from the base, that fall directly into the soil.

409   Another discrepancy exists in the relationship between measured ^{10}Be concentrations and

410   protrusion heights of our sampled boulders. No significant relationship exists between protrusion

411   height and ^{10}Be concentration for all samples plotted together (Fig. 5C); this is to be expected as

412 each individual site has a unique local denudation rate. On the other hand, one would expect a

413 relationship between protrusion and concentration for boulders sampled from the same site (i.e. at

414 Cerro Anay ridge in NA, and Santa Gracia Hill and Zebra Hill in SG). At Santa Gracia Hill and

415 Zebra Hill, taller boulders have a higher [10]Be concentration, as expected, but the highest-

416 protruding boulder sample from Cerro Anay has a lower concentration than the second-tallest

417 sample, perhaps due to toppling of pieces of the tallest boulders. The differential erosion rate

418 between boulders and soil at Cerro Anay ridge is also one of the highest for NA at 5 m Myr^{-1}

419 (Table 2), indicating relatively rapid exposure of boulders that may raise the risk of boulder

420 toppling. However, there is an overlap in the modelled denudation rates of all three boulder and

421 soil sample pairs from Cerro Anay ridge (Fig. 6A).

422   The lack of a trend between boulder protrusion height and [10]Be concentration could also

423 be due to changing soil denudation rates over time. Taller boulders and boulders with longer

424 residence times (such as those on the slope of Cerro Anay Hill in NA and the slope of Santa

425 Gracia Hill in SG; Table 2), were exhumed during one or more glacial-interglacial cycles; during

426 such climatic transitions, soil denudation rates could have changed. Similarly, Raab et al. (2019)

427 suggested that soil denudation rates surrounding tors in southern Italy shifted in conjunction with

428 climate changes over the course of their exhumation (around 100 ka). However, our approach

429 yields an average soil denudation rate over the time of boulder exhumation; therefore, we can

430 only speculate whether soil denudation rates were variable. Carretier et al. (2018) analyzed

431 denudation rate data for Chile averaged over decadal and millennial timescales, and found that

432 millennial denudation rates are higher than decadal erosion rates, with the highest discrepancy

433 between integration time periods being in the arid north. However, the authors suggest that this

434 discrepancy is related to increased stochasticity of erosion in arid regions; millennial erosion rates

435   reflect many stochastically erosive events, such as 100-year floods, that decadal rates do not

436   record.

437   Given the above caveats and uncertainties, we attempted to identify the most plausible

438   range of denudation rates for each sample type and location for all modelled denudation rates.

439   Specifically, we identified most plausible denudation rate ranges for samples on Cerro Anay

440   ridge and Casa de Piedras based on their overlap with each other, for samples on Cerro Anay

441   slope based on their overlap with sample NA9 on Cerro Anay ridge, and ranges for Santa Gracia

442   hill ridge and slope and Zebra Hill ridge based on the overlap of modelled rates for each location,

443   respectively (Fig. 6). For LC we regard denudation rates near the center of the modelled curves in

444   Figure 5 to be most plausible, based on reasonable expectations of differential erosion (section

445   4.2), and considering possible issues with shielding and toppling (section 5.1). These ranges are

446   listed in Table 2 along with measured and modelled ^{10}Be concentrations of soil samples, and are

447   displayed in Fig. 8 along with previously published soil (Schaller et al., 2018) and catchment-

448   average denudation rates (van Dongen et al., 2019). In the following section, we discuss the

449   erosional processes that may account for the differences and similarities in denudation rates from

450   bedrock, boulders, soil (this study and Schaller et al., 2018), and stream sediment (van Dongen et

451   al., 2019) within each field site.

452   **5.2   Processes controlling differential erosion**

453   **5.2.1   Nahuelbuta (NA)**

454   In NA, (based on the modelled denudation rates that we regard to be most plausible), the

455   slowest denudation rates occur on bedrock and boulders, likely because precipitation runs off

456   quickly from exposed bedrock, limiting its chemical alteration (Eppes and Keanini, 2017) and

457   weathering (Hayes et al., 2020), whereas soils erode faster. However, denudation rates for soil

458   surrounding the sampled boulders are lower than denudation rates from the soil pit and the

459   catchment average denudation rates. It is possible that boulders physically block soil from being

460   transported downslope: where a dense clustering of exhumed boulders exists, the regolith will be

461   thinner, and the boulders may retard soil erosion throughout the area in which they are clustered

462   (Glade et al, 2017). Considering boulder protrusion and modelled differential erosion rates,

463   boulders in NA are exposed over a long period (up to 640 Kyr), allowing time to affect the long-

464   term transportation of surrounding soil downslope. Although we did not measure sediment

465   damming upslope of boulders in the field, we did note a small amount of sediment damming for

466   boulders on slopes. Away from exhumed boulders, where soil is thicker and where slopes are

467   steep enough, shallow landsliding can occur, as observed in NA by Terweh et al. (2021). In

468   accordance with these observations, van Dongen et al. (2019) found that smaller grains in stream

469   sediment were likely derived from the upper mixed soil layer, and the largest grains were likely

470   excavated from depth, perhaps by shallow landsliding. The smaller grains have denudation rates

471   similar to those presented in this study (Fig. 8), while larger grains have denudation rates similar

472   to deeper soil pit samples from Schaller et al. (2018).

473   Finally, in NA, where bedrock fracture density is higher, denudation rates are also higher

474   (Fig. 8), likely because precipitation infiltrates into fractures, accelerating chemical weathering,

475   regolith formation (St. Claire et al., 2015; Lebedeva and Brantley, 2017), and subsequent

476   vegetation growth, which introduces biotic acids that further accelerate chemical weathering

477   (Amundson et al., 2007). We further speculate that large exhumed boulders in NA are also sites

478   of less-fractured bedrock at depth, as boulders can only be as large as the local fracture spacing

479   allows (e.g. Sklar et al., 2017). Based on the observed differences in soil, boulder, and fractured

480   bedrock denudation rates in NA, and on previous studies that have correlated higher fracture

481   density with more rapid erosion (e.g., Dühnforth et al., 2010; Dibiase et al., 2018; Neely et al.,

482   2019), we suggest that bedrock fractures have an effect on NA's morphology through grain size

483   reduction and differential erosion. Further, the thicker soil cover and shallow landsliding on NA

484   slopes may increase the discrepancy between slowly-eroding bedrock and boulders versus more

485   rapidly-eroding, vegetation-covered hillslopes, eventually causing bedrock and boulders to sit at

486   topographic highs, as we observed in the field.

5.2.2   La Campana (LC)

488   In LC we observe the largest range of denudation rates between bedrock, boulders, soil,

489   and stream sediment, and also the highest overall denudation rates of the three field sites. We

490   suspect that both of these characteristics are related to slope angles, which are on average nearly

491   twice as steep as in NA and SG (Table 1; van Dongen et al., 2019). It should be noted that the

492   stream sediment samples were taken from an adjacent catchment that does not drain the hillslopes

493   sampled in this study, and the generally low and wide-ranging [10]Be concentrations in the stream

494   sediment have been related to relatively recent landslides observed in the upper headwaters (van

495   Dongen et al., 2019; Terweh et al., 2021). However, steep slopes are pervasive throughout LC

496   and lead us to suggest that shallow landslides are important erosional processes in this field site.

497   In LC we frequently observed boulder samples with lower [10]Be concentrations than

498   adjacent soil samples (Table 1, section 5.1), which is inconsistent with our simple model of

499   boulder exhumation (Fig. 3), and is possibly because the sampled boulders were not exhumed in

500   situ (section 5.1.1). Landslides as observed in LC can bring down boulders in the processes of

501   downhill movement, and may cause the excavation of larger blocks from greater depth before

502   their size is reduced in the weathering zone. More vigorous mass wasting is consistent with larger

503   average hillslope grain sizes for LC, as compared to NA and SG (Terweh et al., 2021). In general,

504   the high relief, steep slopes, and high denudation rates suggest that tectonic uplift rates in LC

505 could be higher than assumed for the nearby coast (Melnick, 2016). Modelled differential

506 denudation rates between boulders and soil are the highest of all field sites, and therefore the time

507 needed to reach the measured boulder protrusion heights is the lowest (23 and 7 Kyr; Table 2),

508 suggesting relatively rapid turnover of boulder exposure and movement downslope. However, we

509 did note some sediment damming by boulders on LC slopes (Fig. 2B3), and in all cases in LC the

510 modelled soil denudation rates are lower than measured soil denudation rates, suggesting that

511 boulders are locally suppressing soil denudation to some extent on LC slopes.

512   Finally, although the role that fracturing plays in LC is difficult to assess, note that our

513 bedrock sample has a significantly lower denudation rate than boulders and soils (Fig. 8), despite

514 being on a steep slope (Table 1). Rolling and toppling processes that may be relevant for LC

515 boulders are highly unlikely for the bedrock patch, allowing its nuclide concentration to be high.

516 Likewise, the boulder denudation rate from the ridge sample LC1, where the risk of toppling is

517 likely the lowest, is similar to the bedrock denudation rate. Additionally, LC's mediterranean

518 climate features frequent fires, which cause spalling of flakes off rock surfaces. While LC

519 boulders are surrounded by shrubs that occasionally burn, causing spalling of boulder surfaces,

520 the extensive bedrock patch in LC is free of vegetation and therefore at a lower risk for fire-

521 induced erosion.

522 **5.2.3   Santa Gracia (SG)**

523   In the semi-arid landscape of SG, as in humid-temperate NA, boulders are eroding more

524 slowly than the surrounding soil, but the differences in boulder and soil denudation rates are

525 subtle. This leads to a slow exposure of hillslope boulders, with exposure of current boulder

526 protrusion (based on differential modelled denudation rates) taking up to 870 Kyr (Table 2). In

527 addition, denudation rate differences between ridge and slope samples – possibly related to slope

528   angle – are larger than the differences between boulders and soil. Furthermore, unlike in NA, our

529   boulder and soil denudation rates are within the same range as the soil pit and catchment average

530   denudation rates (Fig. 8), suggesting that erosional efficiencies are similar across different

531   sediment sizes. Van Dongen et al. (2019) also measured relatively constant catchment average

532   ^{10}Be concentrations over seven grain size classes in SG (Fig. 8), which suggests that all grain

533   sizes have been transported from the upper mixed layer of hillslope soil and that deep-seated

534   erosion processes are unlikely, in accordance with absent landsliding (Terweh et al., 2021). Thus,

535   our results agree with previous findings that erosion in SG is likely limited to grain-by grain

536   exfoliation of boulders and the slow diffusive creep of the relatively thin soil cover on hillslopes

537   (Schaller et al., 2018). When bedrock is exhumed, its long residence time on hillslopes allows it

538   to weather slowly in place and reduce in size, with minimal transportation of weathered material

539   by runoff and a low degree of chemical weathering and soil production (Schaller and Ehlers,

540   2022).

541   Such a narrow range of relatively low denudation rates indicates that very long time

542   periods are necessary to produce relief between hilltops and valleys. Note, however, despite low

543   uplift rates in SG, the total mean basin slope in SG is 17° compared to 9° in NA (van Dongen et

544   al., 2019). This could be due to low MAP resulting in a low erosional efficiency in SG, which, in

545   order to achieve denudation rates that match uplift rates, requires the slopes to be steeper

546   (Carretier et al., 2018). Although the differences in denudation rates between grain sizes is subtle

547   in SG, soils have higher denudation rates than the boulders they directly surround. Additionally,

548   the measured denudation rates of soil surrounding boulders on SG slopes are lower than modeled

549   soil denudation rates (Table 2), indicating that boulders may be prolonging the residence time of

550   the surrounding soil by a small amount, either by blocking its movement downslope or by

551   contributing grains through exfoliation.

5.3   Fracture control on larger-scale landscape evolution

552

553   We have shown that, in our field sites, bedrock erodes the slowest, followed by boulders,

554   and finally soil. In each climate zone, and especially where chemical weathering plays a large

555   role (NA), sediment size is likely controlled by the spacing of bedrock fractures. Once on the

556   surface, large boulders initially delineated by fracture spacing are more difficult to transport than

557   smaller sediment, and therefore locally retard denudation rates. On the landscape scale, such

558   differential erosion should lead to landscape morphologies controlled by fracture spacing

559   patterns. In NA, we were able to measure fracture density in several bedrock outcrops and found

560   that average higher fracture density per sample site is correlated with higher denudation rates

561   (Fig. 5A). It is plausible that the measured fracture spacing in bedrock outcrops represents the

562   parts of the landscape where bedrock fracture density is the lowest, and it is highest under the soil

563   mantled parts of the landscapes, where fractures are not exposed. We also measured the

564   dimensions of 141 boulders in NA and found that, although there is overlap, the distribution of

565   boulder sizes sits at the left tail of the distribution of 47 fracture spacing measurements (Fig. 5B),

566   indicating that boulders have reduced in size in the weathering zone prior to and during

567   exhumation. If we assume that hillslope sediment lies on a spectrum with unweathered blocks

568   delineated by fractures on one end, and sediment that has been significantly reduced in size in the

569   weathering zone on the other end (e.g. Verdian et al., 2021), boulders in NA seem to fall

570   somewhere in the middle.

571   Bedrock fracture patterns also likely affect stream incision in a similar way, by dissecting

572   bedrock and reducing sediment size, making it easier to be transported by flowing water. This

573   phenomenon may be visible in our field sites on a larger scale, through the similarity of fault and

574   stream orientations. As tectonically-induced faults and fractures are products of the same regional

575   stresses, we assume that regional faults have orientations consistent with fractures in our field

576   sites (c.f., Krone et al., 2021). Regional faults and smaller fractures have been shown to be

577   closely related: Rodriguez Padilla et al. (2022) mapped fractures resulting from the 2019

578   Ridgecrest earthquakes in bedrock and sediment-covered areas, and found that fracture density

579   decreases from main faults with a power law distribution. They also found that the orientations of

580   faults and fractures were closely matching. Fracture orientation has also been shown to influence

581   stream orientation. Roy et al. (2015) modeled stream incision in a landscape dissected by dipping

582   weak zones, meant to resemble fracture or fault zones, and found that in cases with a large

583   contrast in bedrock weakness (>30x), channels migrated laterally to follow the shifting

584   exhumation of the weak zone. In our field sites, we observe that stream channels ($A_{min} \geq 10^5 \, m^2$)

585   generally follow fault orientations (Fig. 7). This is especially clear in SG, where the north-south

586   striking Atacama Fault System is reflected in the orientation of faults, streams, and also fractures

587   measured in a nearby drill core (Krone et al., 2021; Fig. 7). In LC and NA, despite more variety

588   in fault and stream orientations, streams closest to the field sites tend to align with fault

589   orientations (Fig. 7). Especially in NA, the larger streams are often nearly perpendicular to each

590   other, similar to rectangular drainage networks, which are often indicative of structural control on

591   drainage patterns (e.g., Zernitz, 1932). We speculate that over geologic time scales, smaller

592   streams are more transient features, whereas the larger ones are more persistent. These results

593   suggest that within the same rock type, local fracture patterns induced by regional faults can

594   induce differential denudation in landscapes.

595   In summary, we argue that in NA, and possibly also in SG and LC, bedrock fracturing

596   influences landscape morphology by setting grain size and thus dictating patterns of denudation

597   rates on hillslopes and in streams: in situ hillslope boulders likely originated as blocks set by

598   fracture spacing, and after being exhumed, locally suppress denudation as described above. This

599   interpretation is supported by work in Puerto Rico; Buss et al. (2013) studied corestones from two

600   boreholes cutting through regolith in the Luquillo Experimental Forest, and found that corestones

601   decreased in size with increased chemical weathering and exhumation through the regolith

602   profile. They deduced that the corestones likely started as bedrock blocks delineated by fractures.

603   Further, they found that the borehole drilled near a stream channel contained more highly-

604   fractured bedrock compared to the borehole drilled at a ridge, and inferred that corestone size was

605   larger under the ridge due to lower bedrock fracture density. In accordance with Fletcher and

606   Brantley (2010), they concluded that, if erosion and weathering increase with bedrock fracture

607   density, then the ridges and valleys in their study area could be controlled by fracture density

608   patterns.

609   We therefore offer the following conceptual model: in a landscape with fractured bedrock

610   (Fig. 9A), areas with higher fracture density should be sites of smaller hillslope sediment sizes

611   (e.g. Sklar et al., 2017; Neely and Dibiase, 2020), where rainfall can easily infiltrate, conversion

612   of bedrock to regolith is easiest (St. Claire et al., 2015; Lebedeva and Brantley, 2017), and

613   denudation rates are highest. Over time, precipitation will divergently run off topographic highs

614   and starve bedrock and larger boulders on high points while infiltrating into topographic lows,

615   where streams eventually incise (Bierman, 1994; Hayes et al., 2020; Fig. 9B). Bedrock and

616   boulders on topographic highs erode more slowly than finer sediment and soil, accentuating any

617   elevation differences. Regolith instead, also promotes vegetation growth, which slows runoff,

618   raises rates of infiltration, and enhances chemical weathering (Amundson et al., 2007; Fig. 9B).

619   Additional fractures due to topographic stresses from exhumation may form at topographic highs

620   as the topography emerges (St. Claire et al., 2015), countering this positive feedback loop (Fig.

621   9C). Over longer timescales, bedrock with different patterns of fracture density may be exhumed,

622   which can invert landscapes to reflect the new fracture patterns exposed at the surface (Roy et al.,

623   2016). In this way, fracturing, climate, and residence time can operate in conjunction to set the

624   sediment size and morphology of hillslopes and streams within landscapes.

625   To further understand the impact of bedrock fracture density on differential denudation in

626   soil-covered areas, future studies should use other sampling strategies and methods, for example,

627   sampling for cosmogenic radionuclide analysis from hillslopes near road cuts where fractures are

628   visible, pairing such hillslope sampling with geophysical surveys and drill cores, or documenting

629   bedrock cover on ridges versus hillslopes over a wide area.

630   **6   Conclusions**

631   In this study, we explored the ability of bedrock patches and large boulders to retard

632   denudation and influence landscape morphology, in three relatively slowly-eroding landscapes

633   along a climate gradient in the Chilean Coastal Cordillera with different erosional regimes. Based

634   on *in situ* cosmogenic ^{10}Be-derived denudation rates of bedrock, boulders and soil, we find that in

635   almost all cases across the three sites studied, soil denudation rates are by ~10-50% higher than

636   the denudation rates of the boulders that they surround, which are more similar to bedrock

637   denudation rates. This pattern is more complicated in La Campana, where some boulders have

638   lower ^{10}Be concentrations than the surrounding soil, perhaps because they were overturned or

639   covered with soil at some point. These results suggest that exposed bedrock patches and large

640   hillslope boulders affect landscape morphology by slowing denudation rates, eventually forming

641   the nucleus for topographic highs. On the other hand, our work also suggests that where slopes

642   are close to the angle of repose and where landsliding is observed (as in La Campana), while

643   bedrock patches erode slowly and likely retard hillslope denudation, hillslope boulders may have

644   a smaller or even negligible effect on suppressing denudation.

645   In addition, we found that bedrock fracturing and faulting accelerates hillslope denudation

646 and stream incision in our field sites: hillslope denudation rates increase with fracture density in

647 NA, and streams tend to follow the orientation of larger faults in all three sites. We infer that

648 bedrock fracture patterns in our field sites set grain sizes on hillslopes, and bedrock patches and

649 boulders represent locations where fracture density is lower, and thus weathering, erosion, and

650 soil formation are suppressed. On a larger scale, our results imply that tectonic preconditioning

651 in the form of bedrock faulting and fracturing influences landscape evolution by impacting the

652 pathway of streams, as well as the migration of ridges, as landscapes erode through layers of

653 bedrock preconditioned by tectonic fracturing over time, and encounter varying levels of

654 resistance depending on the fracture density.

7   Acknowledgements

656   This work was supported by the German Science Foundation (DFG) priority research

657 program SPP-1803 "EarthShape: Earth Surface Shaping by Biota" (grant SCHE 1676/4-2 to D.

658 S.). We are very grateful to the Earthshape management, Friedhelm von Blanckenburg and Todd

659 Ehlers, and the Earthshape coordinators Kirstin Übernickel and Leandro Paulino. We also thank

660 the Chilean National Park Service (CONAF) for providing access to the sample locations and on-

661 site support of our research. We also thank Iris Eder and David Scheer for their help in the field

662 and in the laboratory, Cathrin Schulz for her help in the laboratory, and Steven A. Binnie and

663 Stefan Heinze from Cologne University for conducting AMS measurements.

8   Data Availability

665   Cosmogenic nuclide data and Matlab-scripts of the model presented in this paper will be

666 made available as a GFZ Data Publication in accordance with FAIR principles. LiDAR data from

667 the studied catchments is available in Krüger et al. (2022).

9   References

668

669   Amundson, R., Richter, D. D., Humphreys, G. S., Jobbágy, E. G., and Gaillardet, J.: Coupling

670   between biota and earth materials in the critical zone, Elements, 3 (5), 327-333,

671   https://doi.org/10.2113/gselements.3.5.327, 2007.Alaska Satellite Facility Distributed Active

672   Archive Center: ALOS PALSAR_Radiometric_Terrain_Corrected_high_res

673   (ALPSRP191976520), includes Material © JAXA/METI 2009, ASF DAAC [dataset],

674   https://doi.org/10.5067/Z97HFCNKR6VA, 2009.

675   Alaska Satellite Facility Distributed Active Archive Center: ALOS

676   PALSAR_Radiometric_Terrain_Corrected_high_res (ALPSRP269644390), includes Material ©

677   JAXA/METI 2011, ASF DAAC [dataset], https://doi.org/10.5067/Z97HFCNKR6VA, 2011.

678   Alaska Satellite Facility Distributed Active Archive Center: ALOS

679   PALSAR_Radiometric_Terrain_Corrected_high_res (ALPSRP277746590), includes Material ©

680   JAXA/METI 2011, ASF DAAC [dataset], https://doi.org/10.5067/Z97HFCNKR6VA, 2011.

681   Attal, M., Mudd, S. M., Hurst, M. D., Weinman, B., Yoo, K., and Naylor, M.: Impact of change

682   in erosion rate and landscape steepness on hillslope and fluvial sediments grain size in the Feather

683   River basin (Sierra Nevada, California), Earth Surf. Dynam., 3, 201–222.

684   https://doi.org/10.5194/esurf-3-201-2015, 2015.

685   Balco, G., Stone, J. O., Lifton, N. A., and Dunai, T. J.: A complete and easily accessible means of

686   calculating surface exposure ages or erosion rates from 10Be and 26Al measurements, Quat.

687   Geochronol., 3, 174–195, https://doi.org/10.1016/j.quageo.2007.12.001, 2008.

688   Balco, G., Purvance, M.D. and Rood, D.H.: Exposure dating of precariously balanced rocks,

689   Quat. Geochronol., 6(3-4), 295-303, https://doi.org/10.1016/j.quageo.2011.03.007,

690   2011.Bierman, P.: Using in situ produced cosmogenic isotopes to estimate rates of Landscape

691   evolution: A review from the geomorphic perspective, J. Geophys. Res.: Solid Earth, 99 (B7),

692   13885-13896, https://doi.org/10.1029/94JB00459, 1994.

693   Boisier, J. P., Alvarez-Garretón, C., Cepeda, J., Osses, A., Vásquez, N., and Rondanelli, R.:

694   CR2MET: A high-resolution precipitation and temperature dataset for hydroclimatic research in

695   Chile, Geophys. Res. Abstr., 20(Vic), 2018–19739, 2018.

696   Borchers, B., Marrero, S., Balco, G., Caffee, M., Goehring, B., Lifton, N., Nishiizumi, K.,

697   Phillips, F., Schaefer, J., and Stone, J.: Geological calibration of spallation production rates in the

698   CRONUS-Earth project, Quat. Geochronol., 31, 188-198,

699   https://doi.org/10.1016/j.quageo.2015.01.009, 2016.

700   Braucher, R., Merchel, S., Borgomano, J., and Bourlès, D.L.: Production of cosmogenic

701   radionuclides at great depth: A multi element approach, Earth Planet. Sc. Lett., 309, (1–2), 1-9,

702   https://doi.org/10.1016/j.epsl.2011.06.036, 2011.

703   Burbank, D. W., Leland, J., Fielding, E., Anderson, R. S., Brozovic, N., Reid, M. R., and Duncan,

704   C.: Bedrock incision, rock uplift and threshold hillslopes in the northwestern Himalayas, Nature,

705   379, 505–510, https://doi.org/10.1038/379505a0, 1996.

706   Buss, H.L., Brantley, S.L., Scatena, F.N., Bazilievskaya, E.A., Blum, A., Schulz, M., Jiménez, R.,

707   White, A.F., Rother, G. and Cole, D.: Probing the deep critical zone beneath the Luquillo

708   Experimental Forest, Puerto Rico, Earth Surf. Proc. Land., 38(10), 1170-1186,

709   https://doi.org/10.1002/esp.3409, 2013.

710   Callahan, R.P., Riebe, C.S., Pasquet, S., Ferrier, K.L., Grana, D., Sklar, L.S., Taylor, N.J.,

711   Flinchum, B.A., Hayes, J.L., Carr, B.J. and Hartsough, P.C.: Subsurface weathering revealed in

712   hillslope-integrated porosity distributions, Geophys. Res. Lett., 47(15),

713   https://doi.org/10.1029/2020GL088322, 2020.

714   Carretier, S., Tolorza, V., Regard, V., Aguilar, G., Bermúdez, M.A., Martinod, J., Guyot, J-L,

715   Hérail, G., and Riquelme, R.: Review of erosion dynamics along the major N-S climatic gradient

716   in Chile and perspectives, Geomorphology, 300, 45-68,

717   https://doi.org/10.1016/j.geomorph.2017.10.016, 2018.

718   Chilton, K.D. and Spotila, J.A.: Preservation of Valley and Ridge topography via delivery of

719   resistant, ridge-sourced boulders to hillslopes and channels, Southern Appalachian Mountains,

720   USA, Geomorphology, 365, 107263, https://doi.org/10.1016/j.geomorph.2020.107263, 2020.

721   Clair, J. St., Moon, S., Holbrook, W.S., Perron, J.T., Riebe, C.S., and Martel, S.J.: Geophysical

722   imaging reveals topographic stress control of bedrock weathering, Geomorphology, 350 (6260),

723   2015.

724   Coira, B., Davidson, J., Mpodozis, C., and Ramos, V.: Tectonic and Magmatic Evolution of the

725   Andes of Northern Argentina and Chile, Earth Sci Rev., 18, 303-332, 1982.

726   Dewald, A., Heinze, S., Jolie, J., Zilges, A., Dunai, T., Rethemeyer, J., Melles, M., Staubwasser,

727   M., Kuczewski, B., Richter, J., Radtke, U., von Blanckenburg, F., and Klein, M.: Cologne AMS,

728   a dedicated center for accelerator mass spectrometry in Germany, Nucl. Instrum. Meth., B 294,

729   18-23, dx.doi.org/10.1016/j.nimb.2012.04.030, 2013.

730   DiBiase, R. A., Rossi, M. W., and Neely, A. B.: Fracture density and grain size controls on the

731   relief structure of bedrock landscapes, Geology, 46 (5), 399–402,

732   https://doi.org/10.1130/G40006.1, 2018.

733   Dietrich, W.E., Bellugi, D.G., Sklar, L.S., Stock, J.D., Heimsath, A.M., and Roering, J.J.:

734   Geomorphic transport laws for predicting landscape form and dynamics, Geophys. Monogr. -

735   American Geophysical Union, 135, 103-132, https://doi.org/10.1029/135GM09, 2003.

736   Dühnforth, M., Anderson, R.S., Ward, D., and Stock, G.M.: Bedrock fracture control of glacial

737   erosion processes and rates, Geology, 38 (5), 423-426, https://doi.org/10.1130/G30576.1, 2010.

738   Eppes, M. C., and Keanini, R..: Mechanical weathering and rock erosion by climate-dependent

739   subcritical cracking, Rev. Geophys., 55 (2), 470-508, https://doi.org/10.1002/2017RG000557,

740   2017.

741   Fletcher, R.C. and Brantley, S.L.: Reduction of bedrock blocks as corestones in the weathering

742   profile: Observations and model, Am. J. Sci., 310(3), 131-164,

743   https://doi.org/10.2475/03.2010.01, 2010.

744   Glade, R. C., Anderson, R. S., and Tucker, G. E.: Block-controlled hillslope form and persistence

745   of topography in rocky landscape, Geology, 45 (4), 311–314, https://doi.org/10.1130/G38665.1,

746   2017.

747   Glodny, J., Graaefe, K., and Rosenau, M.: Mesozoic to Quaternary continental margin dynamics

748   in South-Central Chile (36–42∘ S): the apatite and zircon fission track perspective, Int. J. Earth

749   Sci., 97, 1271–1291, https://doi.org/10.1007/s00531-007-0203-1, 2008.

750   Granger, D. E., Riebe, C. S., Kirchner, J. W., and Finkel, R. C.: Modulation of erosion on steep

751   granitic slopes by boulder armoring, as revealed by cosmogenic 26Al and 10Be, Earth Planet. Sc.

752   Lett., 186, 269-281, https://doi.org/10.1016/S0012-821X(01)00236-9, 2001.

753   Hayes, N. R., Buss, H. L., Moore, O. W., Krám, P., and Pancost, R. D.: Controls on granitic

754   weathering fronts in contrasting climates, Chem. Geol., 535, 119450,

755   https://doi.org/10.1016/j.chemgeo.2019.119450, 2020.

756   Heimsath, A.M., Chappell, J., Dietrich, W.E., Nishiizumi, K. and Finkel, R.C.: Soil production

757   on a retreating escarpment in southeastern Australia, Geology, 28(9), 787-790,

758   https://doi.org/10.1130/0091-7613(2000)28<787:SPOARE>2.0.CO;2, 2000.

759   Kirby, E. and Whipple, K.X.: Expression of active tectonics in erosional landscapes, J. Struct.

760   Geol., 44, 54-75, https://doi.org/10.1016/j.jsg.2012.07.009, 2012.

761   Krone, L.V., Hampl, F.J., Schwerdhelm, C., Bryce, C., Ganzert, L., Kitte, A., Übernickel, K.,

762   Dielforder, A., Aldaz, S., and Oses-Pedraza, R. Perez, J.P.H.: Deep weathering in the semi-arid

763   Coastal Cordillera, Chile, Sci. Rep., 11(1), 1-15, 2021.

764   Kügler, M., Hoffmann, T. O., Beer, A. R., Übernickel, K., Ehlers, T. A., Scherler, D., and Eichel,

765   J.: (LiDAR) 3D Point Clouds and Topographic Data from the Chilean Coastal Cordillera, V. 1.0,

766   GFZ Data Services, https://doi.org/10.5880/fidgeo.2022.002, 2022.

767   Lal, D.: Cosmic ray labeling of erosion surfaces: in situ nuclide production rates and erosion

768   models, Earth Planet. Sc. Lett., 104, 424–439, https://doi.org/10.1016/0012-821X(91)90220-C,

769   1991.

770   Lebedeva, M. I. and Brantley, S. L.: Weathering and erosion of fractured bedrock systems, Earth

771   Surf. Proc. Land., 42, 2090–2108, https://doi.org/10.1002/esp.4177, 2017.

772   Martel, S.J.: Mechanics of curved surfaces, with application to surface-parallel cracks, Geophys.

773   Res. Lett., 38(20), https://doi.org/10.1029/2011GL049354, 2011.

774   Melnick, D.: Rise of the central Andean coast by earthquakes straddling the Moho, Nat. Geosci.,

775   9, 1–8, https://doi.org/10.1038/ngeo2683, 2016.

776   Molnar, P., Anderson, R.S., and Anderson, S.P.: Tectonics, fracturing of rock, and erosion, J.

777   Geophys. Res., 112, F03014, https://doi.org/10.1029/2005JF000433, 2007.

778   Mutz, S.G. and Ehlers, T.A.: Detection and explanation of spatiotemporal patterns in Late

779   Cenozoic palaeoclimate change relevant to Earth surface processes, Earth Surf. Dynam., 7(3),

780   663-679, https://doi.org/10.5194/esurf-7-663-2019, 2019.

781   Neely, A.B., DiBiase, R.A., Corbett, L.B., Bierman, P.R., and Caffee, M.W.: Bedrock fracture

782   density controls on hillslope erodibility in steep, rocky landscapes with patchy soil cover,

783   southern California, USA, Earth Planet. Sc. Lett., 522, 186-197,

784   https://doi.org/10.1016/j.epsl.2019.06.011, 2019.

785 Neely, A.B. and DiBiase, R.A.: Drainage Area, Bedrock Fracture Spacing, and Weathering

786 Controls on Landscape-Scale Patterns in Surface Sediment Grain Size, J. Geophys. Res. Earth

787 Surf., 125, (10), https://doi.org/10.1029/2020JF005560, 2020.

788 Oberlander, T. M.: Morphogenesis of Granitic Boulder Slopes in the Mojave Desert, California,

789 J. Geol., 80, 1–20, https://doi.org/10.1086/627710, 1972.

790 Oeser, R. A., Stroncik, N., Moskwa, L., Bernhard, N., Schaller, M., Canessa, R., Brink, L. Van

791 Den, Köster, M., Brucker, E., Stock, S., Pablo, J., Godoy, R., Javier, F., Oses, R., Osses, P.,

792 Paulino, L., Seguel, O., Bader, M. Y., Boy, J., Dippold, M. A., Ehlers, T. A., Kühn, P.,

793 Kuzyakov, Y., Leinweber, P., Scholten, T., Spielvogel, S., Spohn, M., Übernickel, K., Tielbörger,

794 K., Wagner, D., and von Blanckenburg, F.: Chemistry and microbiology of the Critical Zone

795 along a steep climate and vegetation gradient in the Chilean Coastal Cordillera, Catena, 170, 183–

796 203, https://doi.org/10.1016/j.catena.2018.06.002, 2018.Perron, J.T.: Numerical methods for

797 nonlinear hillslope transport laws, J. Geophys. Res. Earth Surf., 116 (F2),

798 https://doi.org/10.1029/2010JF001801, 2011.

799 Portenga, E.W. and Bierman, P.R.: Understanding earth's eroding surface with 10Be, GSA

800 Today, 21, 4–10, https://doi.org/10.1130/G111A.1, 2011.

801 Raab, G., Egli, M., Norton, K., Dahms, D., Brandová, D., Christl, M. and Scarciglia, F.: Climate

802 and relief-induced controls on the temporal variability of denudation rates in a granitic upland,

803 Earth Surf. Proc. Land., 44(13), 2570-2586, https://doi.org/10.1002/esp.4681, 2019.

804   Roda-Boluda, D.C., D'Arcy, M., McDonald, J., and Whittaker, A.C.: Lithological controls on

805   hillslope sediment supply: insights from landslide activity and grain size distributions, Earth Surf.

806   Proc. Land., 43, 956–977, https://doi.org/10.1002/esp.4281, 2018.

807   Rodriguez Padilla, A.M., Oskin, M.E., Milliner, C.W. and Plesch, A.: Accrual of widespread rock

808   damage from the 2019 Ridgecrest earthquakes, Nat. Geosci., 15(3), 222-226, 2022.

809   Roy, S.G., Tucker, G.E., Koons, P.O., Smith, S.M., Upton, P.: A fault runs through it: Modeling

810   the influence of rock strength and grain-size distribution in a fault-damaged landscape, J.

811   Geophys. Res. Earth Surf., 121, https://doi.org/10.1002/2015JF003662, 2016.

812   Roy, S.G., Koons, P.O., Upton, P. and Tucker, G.E.: The influence of crustal strength fields on

813   the patterns and rates of fluvial incision, J. Geophys. Res, Earth Surf., 120(2), 275-299,

814   https://doi.org/10.1002/2014JF003281, 2015.

815   Schaller, M., Ehlers, T.A., Lang, K.A.H., Schmid, M., and Fuentes-Espoz, J.P.: Addressing the

816   contribution of climate and vegetation cover on hillslope denudation, Chilean Coastal Cordillera

817   (26◦–38◦S), Earth Planet. Sc. Lett., 489, 111–122, https://doi.org/10.1016/j.epsl.2018.02.026,

818   2018.

819   Schaller, M. and Ehlers, T.A.: Comparison of soil production, chemical weathering, and physical

820   erosion rates along a climate and ecological gradient (Chile) to global observations, Earth Surf.

821   Dynam., 10 (1), 131-150, https://doi.org/10.5194/esurf-10-131-2022, 2022.

822   Schwanghart, W. and Scherler, D.: Short Communication: Topo Toolbox 2 – MATLAB-based

823   software for topographic analysis and modeling in Earth surface sciences, Earth Surf. Dynam., 2,

824   1–7, https://doi.org/10.5194/esurf-2-1-2014, 2014.

825   SERNAGEOMIN, Mapa Geológico de Chile: versión digital, Servicio Nacional de Geología y

826   Minería, Publicación Geológica Digital No. 4 [dataset], http://www.ipgp.fr/~dechabal/Geol-

827   millon.pdf, 2003.

828   Shobe, C. M., Tucker, G. E., and Anderson, R. S.: Hillslope-derived blocks retard river incision,

829   Geophys. Res. Lett., 43, 5070–5078, https://doi.org/10.1002/2016GL069262, 2016.

830   Sklar, L. S., Riebe, C. S., Marshall, J. A., Genetti, J., Leclere, S., Lukens, C. L., and Merces, V.:

831   The problem of predicting the size distribution of sediment supplied by hillslopes to rivers,

832   Geomorphology, 277, 31–49, https://doi.org/10.1016/j.geomorph.2016.05.005, 2017.

833   Sklar, L.S., Riebe, C.S., Genetti, J., Leclere, S. and Lukens, C.E.: Downvalley fining of hillslope

834   sediment in an alpine catchment: implications for downstream fining of sediment flux in

835   mountain rivers, Earth Surf. Proc. Land., 45(8), 1828-1845, https://doi.org/10.1002/esp.4849,

836   2020.

837   Small, E.E., Anderson, R.S., Repka, J.L., and Finkel, R.St.: Erosion rates of alpine bedrock

838   summit surfaces deduced from in situ 10Be and 26A1, Earth Planet. Sc. Lett., 150, 413-425,

839   https://doi.org/10.1016/S0012-821X(97)00092-7, 1997.

840   Stone, J.O.: Air pressure and cosmogenic isotope production, J. Geophys. Res. Solid Earth, 105,

841   B10, 23753-23759, https://doi.org/10.1029/2000JB900181, 2000.

842   Terweh, S., Hassan, M.A., Mao, L., Schrott, L., and Hoffmann, T.O.: Bio-climate affects

843   hillslope and fluvial sediment grain size along the Chilean Coastal Cordillera, Geomorphology,

844   384, 107700, https://doi.org/10.1016/j.geomorph.2021.107700, 2021.

845   Thaler, E.A. and Covington, M.D.: The influence of sandstone caprock material on bedrock

846   channel steepness within a tectonically passive setting: Buffalo National River Basin, Arkansas,

847   USA, J. Geophys. Res. Earth Surf., 121(9), 1635-1650, https://doi.org/10.1002/2015JF003771,

848   2016.

849   van Dongen, R., Scherler, D., Wittmann, H., and von Blanckenburg, F.: Cosmogenic 10Be in

850   river sediment: where grain size matters and why, Earth Surf. Dynam., 7, 393–410,

851   https://doi.org/10.5194/esurf-7-393-2019, 2021.

852   van Dongen, R.: Discharge variability and river incision along a climate gradient in central Chile.

853   PhD thesis. Potsdam, Germany, 2021.

854   Verdian, J.P., Sklar, L.S., Riebe, C.S. and Moore, J.R.: Sediment size on talus slopes correlates

855   with fracture spacing on bedrock cliffs: implications for predicting initial sediment size

856   distributions on hillslopes, Earth Surf. Dynam., 9(4), 1073-1090, https://doi.org/10.5194/esurf-9-

857   1073-2021, 2021.

858   von Blanckenburg, F., Hewawasam, T., and Kubik, P.W.: Cosmogenic nuclide evidence for low

859   weathering and denudation in the wet, tropical highlands of Sri Lanka, J. Geophys. Res., 109,

860   F03008, https://doi.org/10.1029/2003JF000049, 2004.

861   Zernitz, E.R.: Drainage patterns and their significance, J. Geol., 40 (6), 498-521,

862   https://doi.org/10.1086/623976, 1932.

863   **10 Tables**

864   Table 1. ^{10}Be cosmogenic nuclide sample data.

Sample ID	IGSN [a]	Sampling location [b]	Latitude (°N)	Longitude (°E)	Sample type [c]	^{10}Be conc. ±2σ (×10^5) (atoms g^{-1})	^{10}Be conc. normalized by SLHL ±2σ (×10^5) (atoms g^{-1}) [d]	^{10}Be production rate (spallation, atoms g^{-1} yr^{-1})	Site scaling factor [e]	Slope angle at sample location (°) [f]	Avg. boulder width / protrusion or fracture density [g]	No. chips taken for sample
							Nahuelbuta					
NB-BR1	GFRD1002U	PdA ridge 1	-37.826	-73.035	BR	8.25±0.56	2.92±0.20	11.41	2.82	18	7.83	20
NB-BR2	GFRD1002V	PdA ridge 2	-37.821	-73.034	BR	6.92±0.48	2.43±0.18	11.44	2.85	4	4.75	15
NB-BR3	GFRD1002W	PdA ridge 3	-37.819	-73.032	BR	5.18±0.40	1.86±0.14	11.15	2.78	3	2	15
NB-BR4	GFRD10029	PdA ridge 4	-37.825	-73.034	BR	3.85±0.28	1.36±0.10	11.46	2.84	16	4.78	15
NA3	GFEL10002	PdA slope	-37.826	-73.034	BR	6.55±0.46	2.38±0.16	11.25	2.75	25	4.43	30
NA4	GFEL10003	CdP	-37.817	-73.031	B	9.08±0.64	3.49±0.24	10.43	2.60	5	1.70 / 0.68	30
NA7	GFEL10006	CA ridge	-37.789	-72.998	B	10.28±0.72	3.65±0.26	11.3	2.81	10	1.52 / 1.00	10
NA8	GFEL10007	CA ridge	-37.789	-72.998	B	8.94±0.62	3.18±0.22	11.3	2.81	10	3.30 / 2.43	10
NA9	GFEL10008	CA ridge	-37.789	-72.998	B	7.57±0.54	2.69±0.18	11.3	2.81	10	0.64 / 0.19	10
NA11	GFEL1000A	CA slope	-37.790	-72.999	B	7.67±0.54	2.76±0.18	11.18	2.78	14	1.90 / 1.60	10
NA15	GFEL1000E	SPH slope	-37.807	-73.013	B	2.84±0.14	1.12±0.06	10.24	2.53	18	0.96 / 0.76	12
NA5	GFEL10004	CdP	-37.817	-73.031	S	2.32±0.20	0.89±0.08	10.43	2.60	5	N/A	N/A
NA10	GFEL10009	CA ridge	-37.789	-72.998	S	5.04±0.36	1.79±0.12	11.3	2.81	10	N/A	N/A
NA12	GFEL1000B	CA slope	-37.790	-72.999	S	4.27±0.32	1.54±0.12	11.18	2.78	14	N/A	N/A
							La Campana					
LC-BR2	GFRD1002X	CC slope	-32.938	-71.081	BR	1.83±0.22	1.38±0.16	5.75	1.33	39	N/A	15
LC2	GFEL1002J	CC ridge	-32.939	-71.081	B	0.92±0.18	0.59±0.12	6.25	1.55	9	0.95 / 0.54	10
LC4	GFEL1003V	CC slope	-32.938	-71.079	B	0.92±0.16	0.66±0.12	5.77	1.40	27	0.30 / 0.15	10
LC11	GFEL1000Q	CG ridge	-32.941	-71.074	B	1.21±0.14	0.76±0.08	6.42	1.59	13	1.32 / 0.70	10
LC13	GFEL1000S	CG upper slope	-32.94	-71.073	B	0.73±0.16	0.51±0.12	6.13	1.43	33	0.32 / 0.20	12
LC18	GFEL1000Z	CG lower slope	-32.937	-71.074	B	1.55±0.16	1.17±0.12	5.43	1.32	18	0.50 / 0.32	12
LC1	GFEL1002H	CC ridge	-32.939	-71.081	S	1.54±0.18	0.99±0.12	6.25	1.55	9	N/A	N/A
LC3	GFEL1003W	CC slope	-32.938	-71.079	S	1.03±0.18	0.74±0.12	5.77	1.40	27	N/A	N/A
LC12	GFEL1000R	CG ridge	-32.941	-71.074	S	0.88±0.08	0.55±0.06	6.42	1.59	13	N/A	N/A
LC14	GFEL1000T	CG upper slope	-32.940	-71.073	S	0.63±0.08	0.44±0.06	6.13	1.43	33	N/A	N/A
LC19	GFEL1000X	CG lower slope	-32.937	-71.074	S	1.84±0.14	1.39±0.10	5.43	1.32	18	N/A	N/A
							Santa Grácia					
SG8	GFEL10017	SGH ridge	-29.756	-71.166	B	5.94±0.42	4.17±0.30	5.72	1.42	10	1.10 / 0.80	10
SG9	GFEL10018	SGH ridge	-29.756	-71.166	B	4.70±0.34	3.30±0.24	5.72	1.42	10	0.38 / 0.12	10
SG11	GFEL1001A	SGH slope 1	-29.758	-71.166	B	3.56±0.26	2.61±0.20	5.56	1.36	21	1.30 / 0.87	9
SG22	GFEL1001M	SGH slope 2	-29.758	-71.166	B	3.85±0.30	2.83±0.22	5.56	1.36	22	0.37 / 0.24	11
SG37	GFEL1002T	ZH ridge	-29.740	-71.156	B	11.46±0.88	8.21±0.62	5.64	1.40	28	1 / 0.90	10
SG38	GFEL1002S	ZH ridge	-29.740	-71.156	B	7.84±0.56	5.62±0.40	5.64	1.40	28	0.10 / 0.12	10
SG10	GFEL10019	SGH ridge	-29.756	-71.166	S	2.58±0.22	1.81±0.16	5.72	1.42	10	N/A	N/A
SG12	GFEL1001B	SGH slope 1	-29.758	-71.166	S	2.39±0.18	1.75±0.14	5.56	1.36	21	N/A	N/A
SG23	GFEL1001N	SGH slope 2	-29.758	-71.166	S	2.10±0.16	1.54±0.12	5.56	1.36	22	N/A	N/A
SG36	GFEL1002U	ZH ridge	-29.740	-71.156	S	5.40±0.50	3.87±0.36	5.64	1.40	28	N/A	N/A

[a]Open access metadata: http://igsn.org/[insert IGSN number here]
[b]Sample locations: PdA: Piedra de Aguila, CdP: Casa de Piedas, CA: Cerro Anay, SPH: Soil Pit Hill, CC: Cerro Cabra, CG: Cerro Guanaco, SGH: Santa Gracia Hill, ZH: Zebra Hill..
[c]Sample type abbreviations: BR: bedrock, B: boulders, S: soil.
[d]Concentrations were normalized to SLHL (sea level high latitude) using a SLHL production rate of 4.01 atoms g-1 yr^{-1} (Borchers et al., 2016) and the site's scaling factor.
[e]Time constant spallation production rate scaling scheme of Lal (1991) and Stone (2000) ('St' in Balco et al., 2008), calculated taking topographic shielding into account.
[f]Local hillslope angles were calculated using a 12.5m DEM and an 8-connected neighbourhood method.
[g]Fracture density for bedrock (in meters) and width and protrusion measurements (in meters) for boulders. Values are averages of >10 measurements per sample site.

Table 2. Modelled denudation rates for soil and boulder samples using the first term of Eq. 1, and comparison of modelled and measured [10]Be concentrations for soil samples. Sample location abbreviations are described in the caption for Table 1.

Sample location	Soil sample ID	Best-fitting modelled soil denudation range rate (ϵ_s) (m Myr^{-1})	Corresp. modelled range of [10]Be conc. (×10^5) (atoms g^{-1}) for soil (N$_m$)	Measured [10]Be conc. ±2σ (×10^5) (atoms g^{-1})	Boulder sample IDs	Best-fitting modelled boulder denudation rate range (ϵ_b) (m Myr^{-1})	Differential erosion rate (boulder vs. soil; m Myr^{-1})	Time needed for boulder exposure (Kyr)
Nahuelbuta								
CdP	NA5	15-20	3.61-4.75	2.32±0.20	NA4	10-15	5	136
CA ridge	NA10	15-20	3.89-5.12	5.04±0.36	NA7, NA8, NA9	10-15	5	200, 486, 38
CA slope	NA12	18-20	3.84-4.25	4.27±0.32	NA11	15-18	2.5	640
La Campana								
CG ridge	LC12	70-90	0.54-0.69	0.88±0.08	LC11	40-60	30	23
CG upper slope	LC14	120-140	0.32-0.37	0.63±0.08	LC13	80-120	30	7
Santa Gracia								
SGH ridge	SG10	12-15	2.77-3.41	2.58±0.22	SG8, SG9	10-12	2.5	320, 48
SGH slope 1	SG12	19-21	1.94-2.13	2.39±0.18	SG11	18-20	1	870
SGH slope 2	SG23	19-21	1.94-2.13	2.10±0.16	SG22	18-20	1	240
ZH ridge	SG36	6.5-7.5	4.78-5.45	5.40±0.50	SG37, SG38	4-5.5	2.25	400, 53

11 Figures
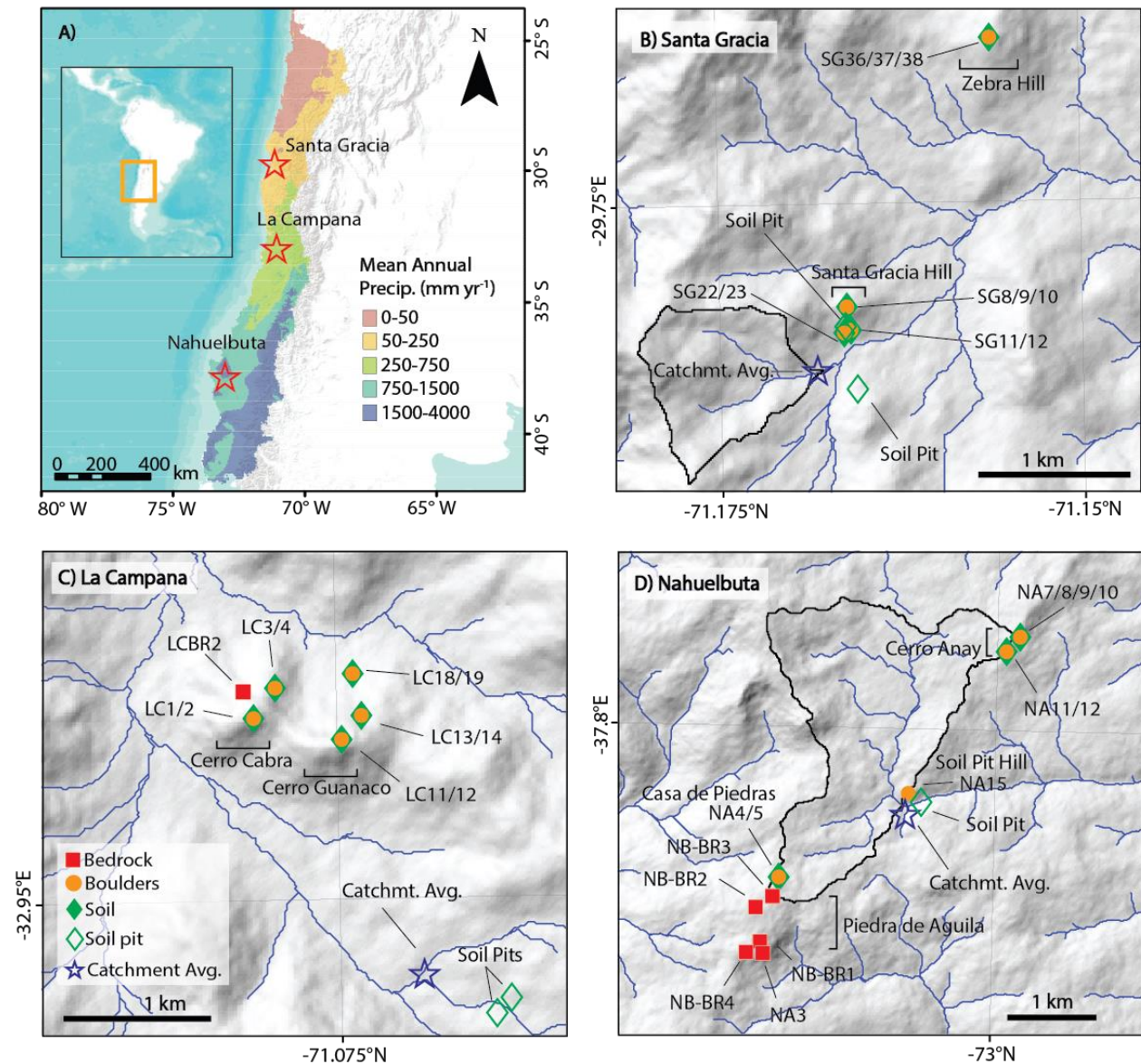
Figure 1. Field site locations and features. A) Map of mean annual precipitation in central Chile, with field sites marked by red stars. Precipitation data from the CR2MET dataset, by the Center for Climate and Resilience Research (CR^2) (Boisier et al., 2018), provides an average for the time period 1979-2019. World Terrain Base map sources are Esri, USGS, NOAA. B-D: Hillshade images from 12.5-m ALOS PALSAR digital elevation models, of B) Santa Gracia (SG), C) La Campana (LC), and D) Nahuelbuta (NA). Sample locations and sample names are shown, with symbol shape and color indicating the sample type (see legend in lower left panel). Black outlines delineate the catchments from which the catchment average sample (star) was taken (the catchment from La Campana does not fit within the bounds of the map and therefore is not shown). Blue lines indicate streams. Soil pit sample data are from Schaller et al. (2018), and catchment average sample data are from van Dongen et al. (2019).
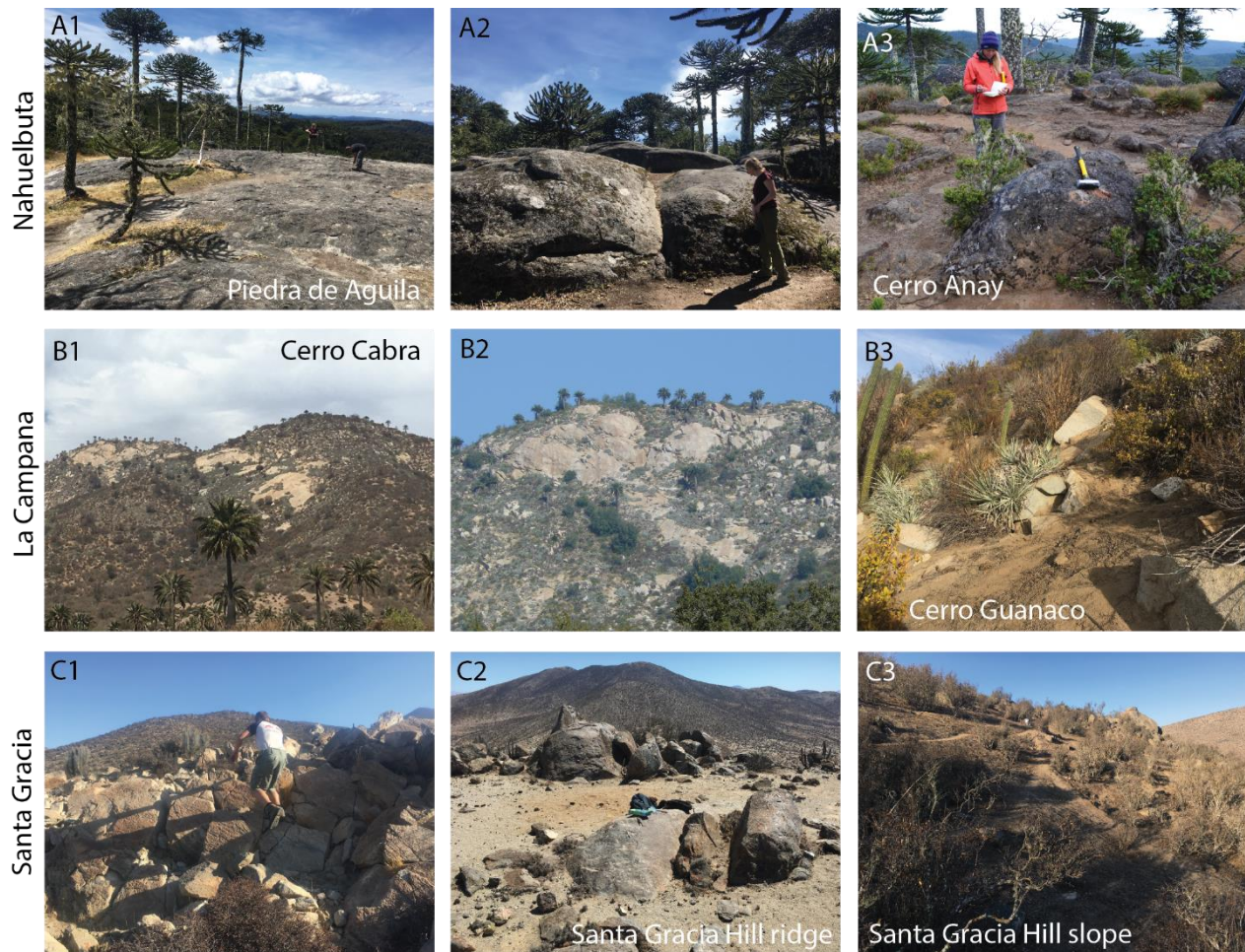
Figure 2. Field photos showing the various surfaces sampled, including bedrock, boulders and soil. A: Nahuelbuta, A1) Bedrock (sample NB-BR1). A2) Fractured bedrock, in transition between unfractured bedrock and boulders (sample NB-BR2). A3) Smaller boulders surrounded by soil (sample NA7). B: La Campana, B1) Bedrock (sample LC-BR2). B2) Bedrock transitioning to large boulders and soil. B3) Boulders and soil on a hillside (samples LC13 and LC14). C: Santa Gracia, C1) Boulders on Zebra Hill delineated by fractures. C2) Large boulders on the ridge of Santa Gracia Hill (sample SG8). C3) Soil with minimal boulders on the slope of Santa Gracia Hill (samples SG22 and SG23).
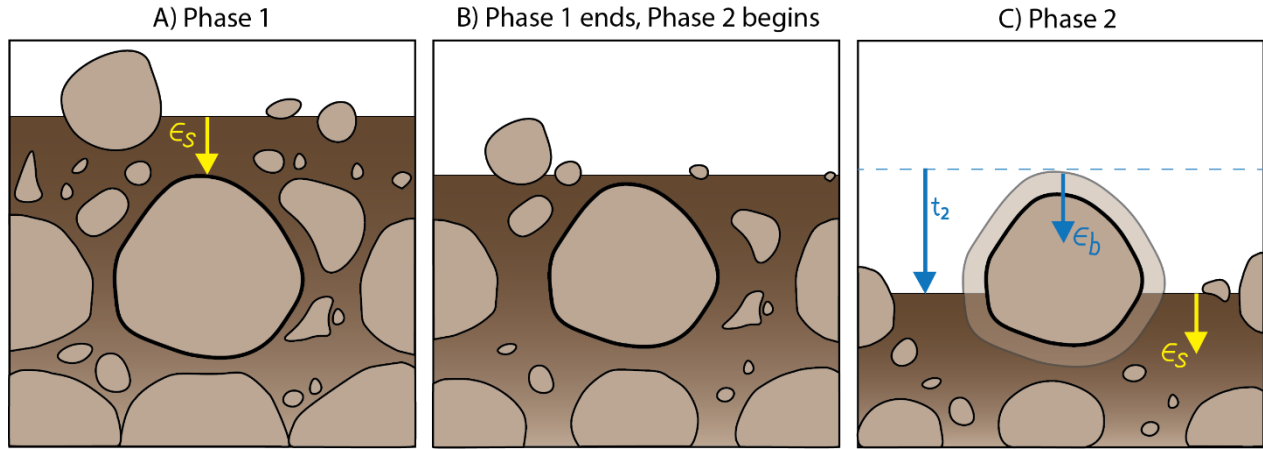
Figure 3. Schematic image showing the process of boulder exhumation. A) Overview of the setting: a mixed soil- and bedrock- covered hillslope where sediment size decreases with decreasing fracture spacing. B) During phase 1, the boulder is buried, and accumulates nuclides at a rate governed by the soil denudation rate, ϵ_s. C) Phase 1 ends when the boulder breaches the soil surface. D) During phase 2, the boulder itself is eroding at a rate of ϵ_b, and the surrounding soil continues to erode at a rate of ϵ_s. Phase 2 lasts for a time period t_2 that ends with our sampling.
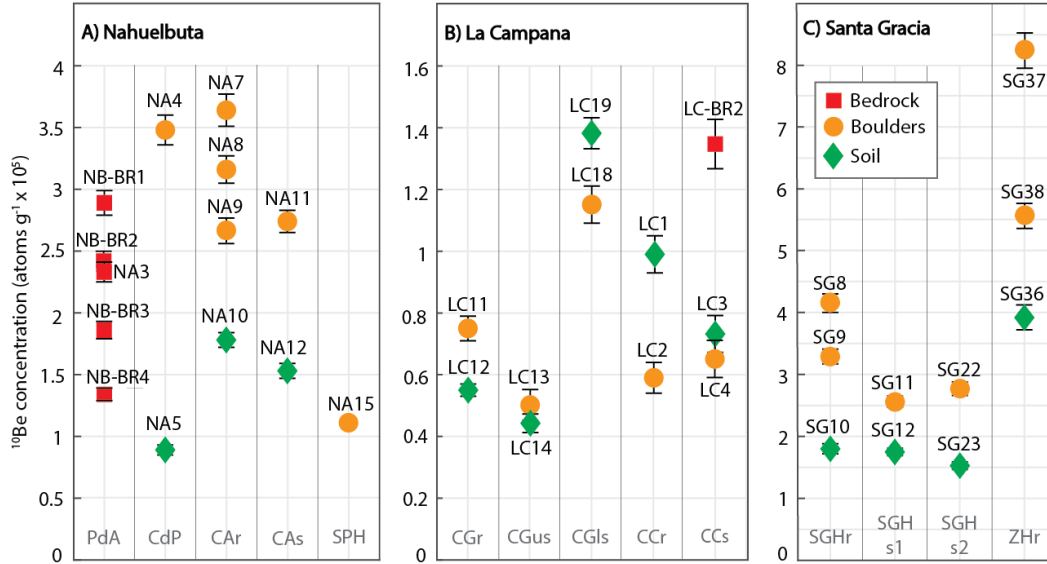
Figure 4. Measured ^{10}Be concentrations normalized to reference production rate at sea-level high latitude for A) Nahuelbuta, B) La Campana, and C) Santa Gracia; note different scales of y-axes. X-axes are not numerical but rather show the sampling locations, also reported in Table 1. Labels next to data points provide sample IDs, also reported in Table 1. Gray labels at the bottom of panels are the sample locations. PdA: Piedra de Aguila, CdP: Casa de Piedas, CAr: Cerro Anay ridge, CAs: Cerro Anay slope, SPH: Soil Pit Hill, CGr: Cerro Guanaco ridge, CGus: Cerro Guanaco upper slope, CGls: Cerro Guanaco lower slope, CCr: Cerro Cabra ridge, CCs: Cerro

Cabra slope, SGHr: Santa Gracia Hill ridge, SGHs1: Santa Gracia Hill slope 1, SGHs2: Santa Gracia Hill slope 2, ZHr: Zebra Hill ridge.
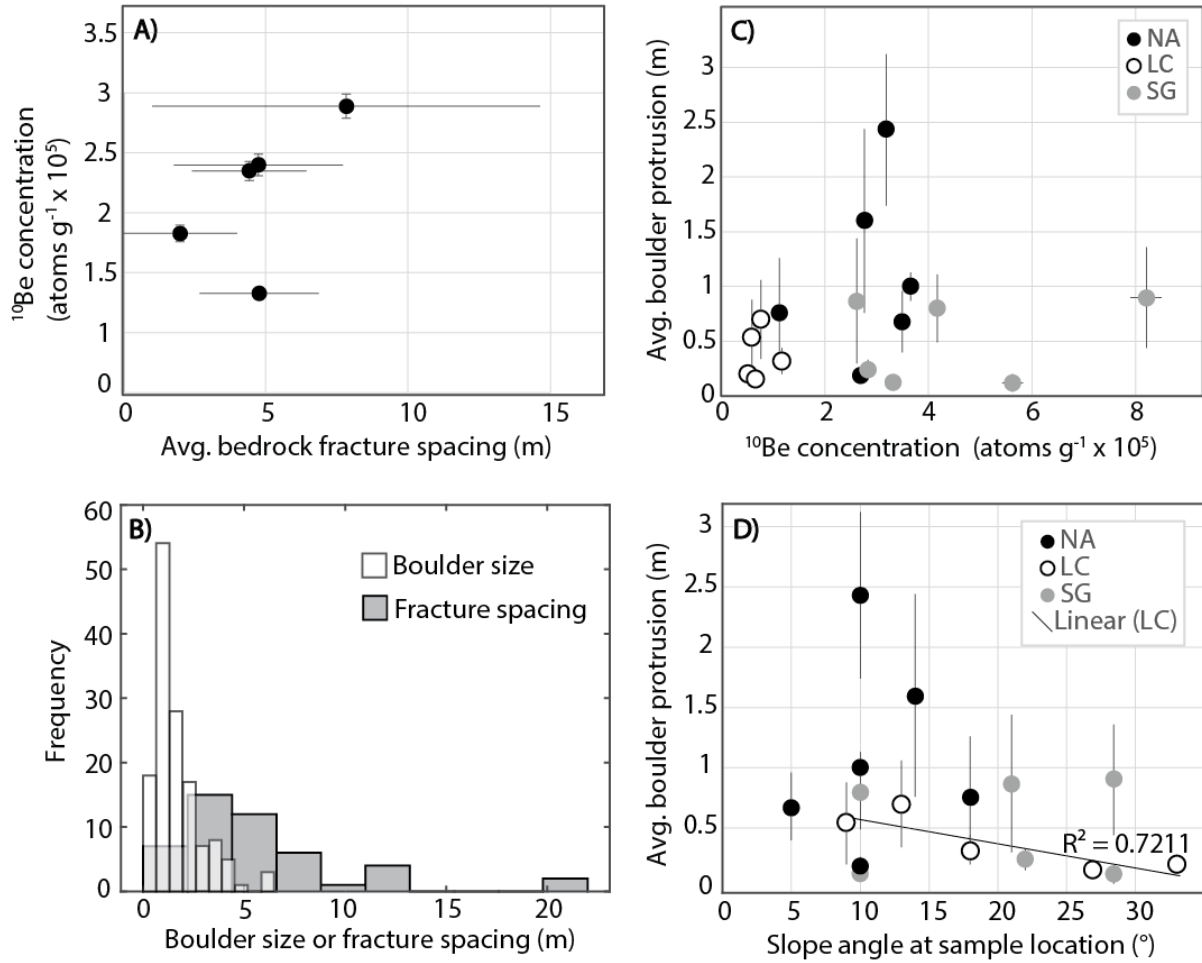
Figure 5. A) Average bedrock fracture spacing (NA only) plotted against measured [10]Be concentrations normalized to reference production rate at sea-level high latitude. Error bars represent the standard deviation of all fracture spacing measurements for each location. B) Measurements of individual fracture spacing and individual boulder sizes, where boulder size is the average of the x and y axes of each boulder, where the z axis is the protrusion height. C) Average boulder protrusion height plotted against measured [10]Be concentrations normalized to reference production rate at sea-level high latitude for each field site. Error bars represent the standard deviation of all boulder protrusion height measurements for each location. D) Average boulder protrusion height plotted against hillslope angle. A linear regression model is fit through LC datapoints.
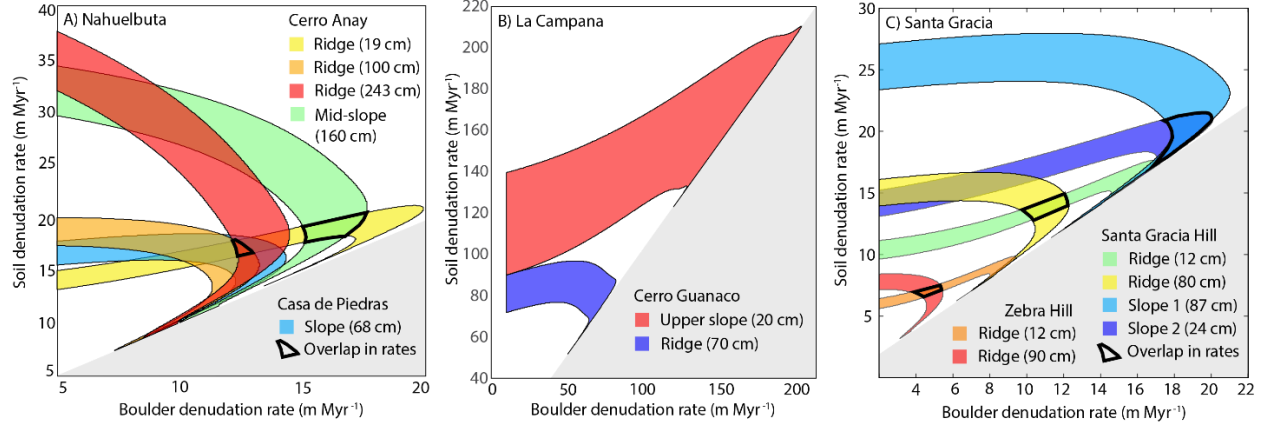
Figure 6. Range of best fitting combinations of modelled soil and boulder denudation rates in A) Nahuelbuta, B) La Campana, and C) Santa Gracia according to Eq. 1. Each color band corresponds to an amalgamated boulder sample, listed in the legend along with the average protrusion height of the boulders. Areas where best fitting denudation rates overlap for samples from the same location are highlighted by a black outline. The gray areas are forbidden fields, as by assumption, boulder denudation rates have to be lower than soil denudation rates, otherwise there would be no boulder protruding above the soil surface.
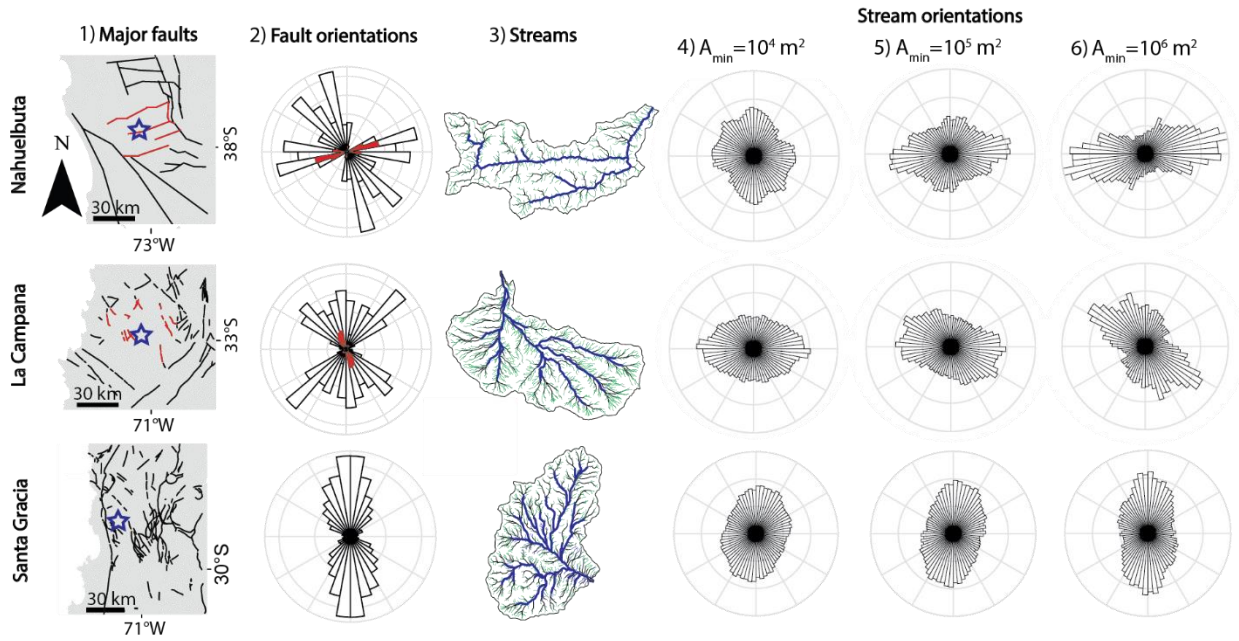
Figure 7. Rose diagram plots and maps showing fault and stream orientations for Nahuelbuta (top row), La Campana (middle row), and Santa Gracia (bottom row). For each field site, the columns show from left to right: (1) major faults digitized from geological map (SERNAGEOMIN, 2003), within ~50 km (black) and ~25 km (red, NA and LC only) of the sampling site (blue star); (2) rose diagram of fault orientations from the maps in column 1, constructed using 100 m long, straight fault segments and 36 bins, with orientations of faults <25 km from NA and LC in red; (3) a map of the studied catchments and the drainage network, with green, black, and blue

streams indicating minimum upstream areas (A_{min}) of 10^4, 10^5, and 10^6 m^2, respectively, derived from one-meter resolution LiDAR DEMs (Kügler et al., 2022).; (4-6) rose diagrams (72 bins) of stream orientations for different A_{min}. All maps and rose diagrams are oriented with the top being north.
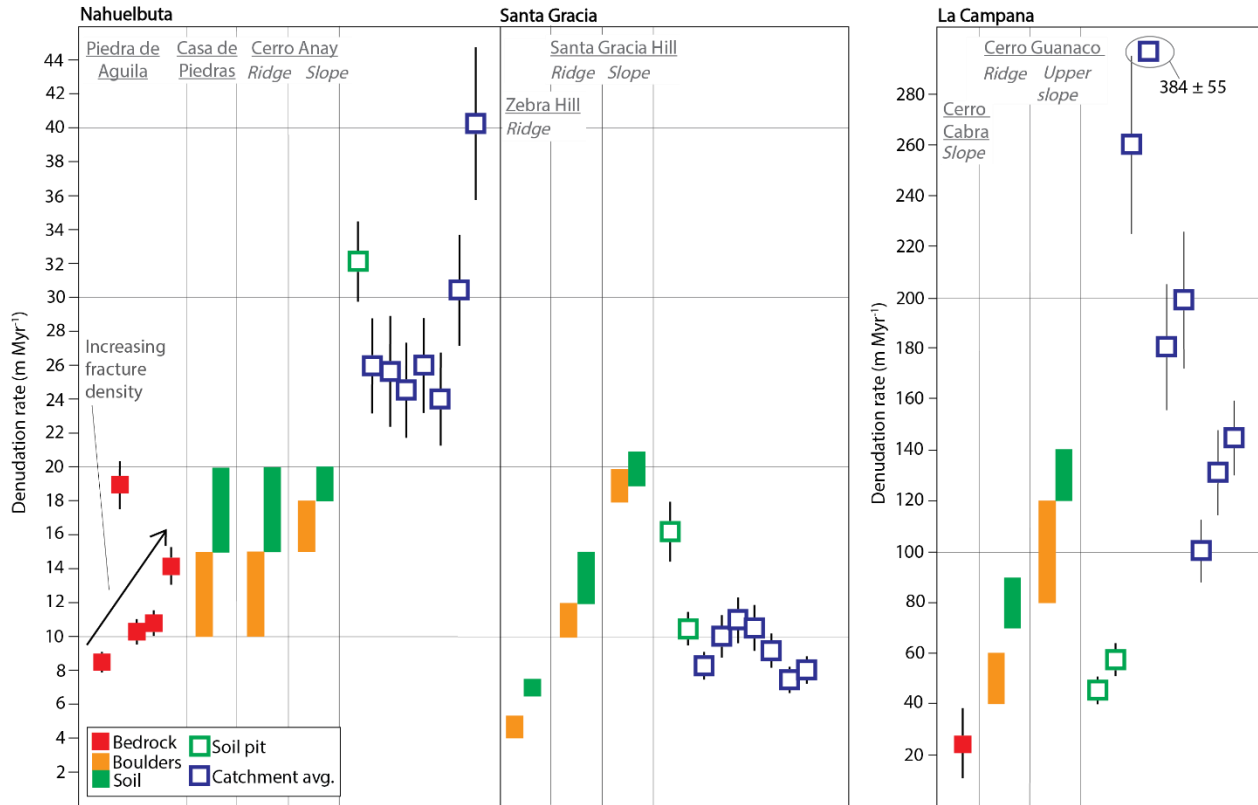
Figure 8. Overview of new and previously published denudation rates (data from this study are shown by solid symbols and previously-published data are shown by hollow symbols). Soil pit data is from Schaller et al. (2018), and catchment average data is from van Dongen et al. (2019). Catchment average denudation rates from various sediment grain sizes (from left to right for each field site: 0.5-1, 1-2, 2-4, 4-8, 8-16, 16-32, and 32-64 mm). Bedrock denudation rates are calculated using the CRONUS online calculator v2.3 (Balco et al., 2008). Boulder and soil denudation rates are estimated using our model and reflect the most plausible denudation rates as described in section 5.1.2. Denudation rates for each location within a field site are separated by thin gray bars, and locations are labeled at the top of the chart. Samples that were not included in the model (one sample from Nahuelbuta and 3 samples from La Campana) are also not included here.
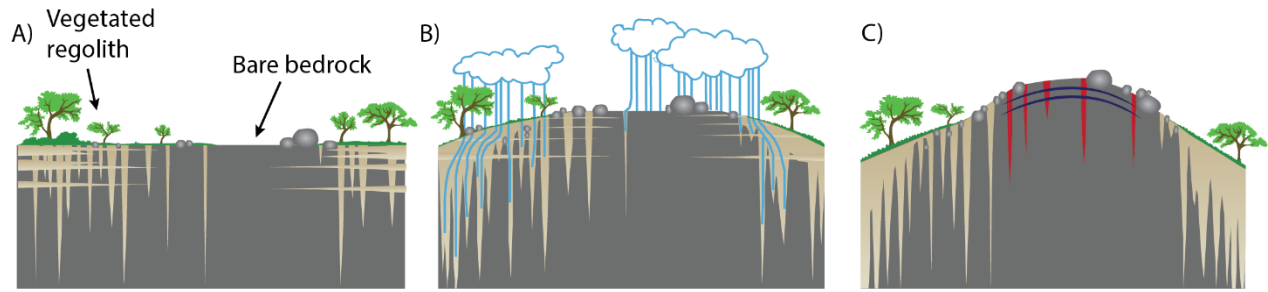
Figure 9. Schematic illustration showing influence of bedrock fractures on landscape evolution. (A) Bedrock with different fracture densities is to different degrees infiltrated by rain and ground water, which leads to differences in chemical weathering, soil formation and vegetation growth, resulting in different hillslope sediment sizes. (B) Differential denudation between highly fractured and less fractured areas induce relief growth under slow but persistent uplift, which further promotes spatial gradients in chemical weathering, hillslope sediment size, and denudation. (C) Growing relief increases topographic stresses and formation of new fractures (red) at topographically high positions (e.g. St. Clair et al., 2015), and non-topographic surface-parallel fractures (dark blue) (e.g. Martel, 2011).